Article:

Hageman, T. orcid.org/0000-0001-7770-7440 and de Borst, R. orcid.org/0000-0002-3457-3574 (2020) Sub-grid models for multiphase fluid flow inside fractures in poroelastic media. Journal of Computational Physics, 414. 109481. ISSN 0021-9991

https://doi.org/10.1016/j.jcp.2020.109481

Sub-grid models for multiphase fluid flow inside fractures in poroelastic media

Tim Hageman, René de Borst*

Department of Civil and Structural Engineering, University of Sheffield, Sheffield S1 3JD, UK

Abstract

Models have been developed for the simulation of multiphase fluid flow within fractured poroelastic media. They allow for the fluid phases to interact inside fractures, without requiring explicit simulations in the interior of the fractures. The models retain the ability to retrieve the fluid velocity profile in the fracture by post-processing. The models for flow within a fracture are combined with a formulation for multiphase flow within the poroelastic medium. They have been implemented using isogeometric analysis, cast into a traditional finite element format using Bézier extraction. Pressure oscillations around the fracture are prevented by using a lumped integration scheme for the pressure capacity. The effect of interactions between the fluid phases is first demonstrated for a single fracture through parameter studies. Next, two cases with a more practical orientation are simulated. They show, *inter alia*, that the inclusion of interactions between the fluid phases can result in fluid back-flow.

Keywords: poroelasticity, multiphase flow, fractured media, isogeometric analysis, fracture flow

---

1. Introduction

Multiphase flow inside fractured poroelastic media is a strongly coupled multi-scale and multi-physics problem. The interstitial fluid inside the porous medium exerts forces on the surrounding solid material, thereby deforming and fracturing the material. In return, the induced volume changes result in pressure changes in the fluid. The introduction of multiple fluids, for instance when simulating oil-ground water interactions or underground CO_2 storage, further increases this coupling by introducing extra interactions between the fluid phases. Fractures in the porous medium introduce additional challenges: A small fracture opening can dominate the fluid transport in the entire porous medium, which is orders of magnitude larger than the fracture opening. Capturing this phenomenon requires an accurate description of the behaviour of the small-scale phenomena inside the fluid-filled fractures. At the same time, the formulation should be capable of simulating large domains. Simulations which include the coupling between a non-fractured porous medium and multiple fluid phases have been carried out using a variety of methods. Finite volume methods have shown their capability of simulating large domains, often including complicated fluid behaviour like capillary and buoyancy based forces [1, 2]. Finite element methods have combined the strengths of methods developed for solid mechanics, incorporating effects due to inertia or plasticity, with formulations for the fluids, either by combining the different models into a single monolithic scheme [3, 4, 5, 6, 7] or by iterating between the solid and fluid solvers[8, 9] [10]. Whereas the finite volume and element methods have focused on including macro-scale behaviour and simulating large domains, pore-scale methods have focused on including the micro-scale behaviour, capturing the behaviour and interactions of the separate fluid phases within the porous media [11, 12, 13]. These pore-scale methods have been used to verify the relations used for other

---

[*] Corresponding author

Email address: `r.deborst@sheffield.ac.uk` (René de Borst)

macro-scale methods, but also to highlight the importance of accurately including micro-scale effects for macro-scale simulations.

Fluid-transporting fractures have been included using the cubic law, originally derived for single-phase flow, combined with an empirical correction factor [14, 15]. These simulations have shown the large effect of the additional fluid transport inside fractures on the overall saturation. A different approach to include this fluid flow has been to model the interior of the fractures as a porous material, assuming large deformations and a variable permeability [16, 17], or by assuming a constant permeability [18, 19, 20, 21]. While all these methods are successful in including the multiphase fluid transport inside the fractures, they assume that both fluid phases coexist within the fracture, without the velocity of one phase influencing that of the other phases. An alternative assumption is assuming immiscible fluids, resulting in the fractures locally only transporting a single phase while keeping track of the location of the interface between the phases [22].

Experiments have shown that interaction between the phases in fractures does occur, however, both in micro-channels with smooth walls [23] and in rough-walled rock joints [24]. Several flow types have been shown to occur, depending on the degree of saturation and on the velocity. As examples we mention bubbly flows, in which the phases are well-mixed, and annular flows, in which the phases form separated layers. Experiments [25] and analytical solutions [26] have shown that these flow types lead to an interaction between the phases, showing counter-current flows and the possibility that one fluid phase is dragged along by another phase.

While it is possible to fully simulate the fluid flow inside the porous medium and inside the fracture [27, 28], this requires the interior of the fracture to be discretised with sufficiently small elements to capture the normal and tangential flow velocities inside the fracture. To avoid these fine meshes, sub-grid models can be used to incorporate the effects of the fracture on the surrounding porous medium. Commonly used models predict the fluid flux within the fracture, and apply this to the surrounding elements, either by directly imposing the flux [29, 30], or altering the permeability [31, 32]. Alternatively, the velocity normal to the fracture, the fracture inflow, can be used to include the effects of the fluid-transporting fractures. This has been used to include fluid-blocking fractures [33] and fluid-transporting fractures with a resistance to flows in the normal direction [34]. By assuming a continuous pressure across the fracture, these fracture inflow models are also able to cover similar cases as the imposed fluid flux models [35, 36].

In this paper, we will derive sub-grid models based on the fracture inflow method. For single-phase flows, these sub-grid models have ~~been derived that are~~ shown to be capable of capturing the physics and behaviour of the fluid inside the fracture without explicitly simulating the interior of these fractures [35, 37, 38] [39, 40, 41, 42]. These models use analytical solutions for the flow within the fracture to impose fracture inflows on the surrounding poroelastic material. The flow in the interior of the fracture can then be reconstructed by post-processing, thus allowing for an accurate determination of the fluid velocities in the fracture [43, 44]. Moreover, it has been proven possible to also consider complex fluids in the interior of the fracture as well as in the surrounding porous medium, for instance non-Newtonian fluids [45, 46], and boundary layers [47, 48], without the need to explicitly simulate this behaviour.

The aim of this study is to extend the aforementioned, physics-based fracture flow models to multiphase flows. The fracture flow models will be incorporated in an isogeometric analysis based finite element method for the poroelastic material. This allows for the simulation of large, fractured domains while retaining the interactions between fluid phases within the small-scale fracture. Two models, for bubbly flow and for separated flow, will be derived and, for comparison with existing models, the cubic law will be cast into a sub-grid fracture flow formulation. The effect of including the interaction between the fluid phases on the resulting saturation will be analysed, and we will highlight the ability of the post-processing to regain the detailed velocity profiles within the fracture. A case containing a single fracture will be simulated to show the relevance of the choice of the model in fracture-flow dominated and in diffusion dominated regimes. Finally, two cases will be presented which are more representative of real applications. They will demonstrate the importance of interactions between the phases on the resulting degrees of saturation.

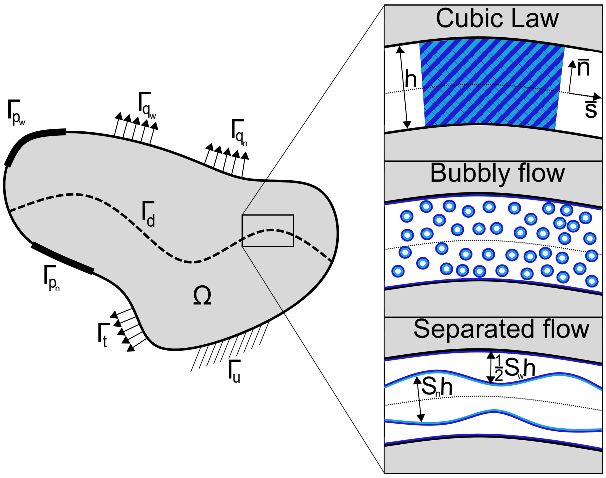

Figure 1: Schematic overview of the porous domain showing boundary conditions, interior discontinuity Γ_d, and the different subgrid models used for the fracture flow including $(\bar{s}, \bar{n})$ coordinate system, definition of fracture height h and for the separated flow the phase heights.

2. Governing equations

A domain Ω consisting of a partially saturated poroelastic material is considered, see Figure 1. The domain is split by an interface Γ_d, which represents a fracture through a C^{-1} discontinuity in the displacements. To allow for fluid transport in the fracture, without explicitly requiring simulation of the flow inside the fracture, a continuous pressure model is used across Γ_d [16]. That is, there is C^0-continuity at the interface for the wetting and non-wetting phase pressures.

2.1. Bulk material

The poroelastic, partially saturated medium is described using the deformations of the porous material $\boldsymbol{u}$, the pressure of the wetting phase p_w and the pressure of the non-wetting phase p_n. The capillary pressure is defined as:

$$p_c = p_n - p_w \tag{1}$$

Based on the capillary pressure, the degree of saturation of the wetting and of the non-wetting phases, S_w and S_n, respectively, can be determined. While many relations exist which describe the relation between the capillary pressure and the degree of saturation [49, 50], an exponential relation describing a water-oil mixture has been chosen here [15]:

$$S_w = e^{-p_c/B} \tag{2a}$$

$$S_n = 1 - S_w = 1 - e^{-p_c/B} \tag{2b}$$

with B an ~~empirical~~ experimentally determined constant.

By assuming the deformations of the solid to occur fast compared to the fluid pressure changes, the system can be considered to react quasi-statically. The deformations of the porous medium are then described by using the momentum balance:

$$\boldsymbol{\nabla} \cdot \boldsymbol{\sigma} = \boldsymbol{0} \tag{3}$$

The total stress $\boldsymbol{\sigma}$ is given by:

$$\boldsymbol{\sigma} = \boldsymbol{\sigma}_s - \alpha \bar{p} \boldsymbol{I} \tag{4}$$

with α the Biot coefficient, and the stress inside the porous medium, $\boldsymbol{\sigma}_s$, assumed to be linearly related to the strain by:

$$\boldsymbol{\sigma}_s = \boldsymbol{D} : \boldsymbol{\varepsilon} \tag{5}$$

with $\boldsymbol{D}$ the elastic fourth order stiffness tensor and $\boldsymbol{\varepsilon} = \boldsymbol{\nabla}^s \boldsymbol{u}$ the infinitesimal strain of the porous material, using $\boldsymbol{\nabla}^s$ to denote the symmetrised gradient operator. The volume-averaged pressure $\overline{p}$ is determined by:

$$\overline{p} = S_w p_w + S_n p_n \tag{6}$$

To describe the interstitial fluid pressure, the mass balances of the porous material, and the wetting and non-wetting phases are used:

$$\frac{\partial (1-n_f)\rho_s}{\partial t} + \boldsymbol{\nabla} \cdot \left((1-n_f)\rho_s \cancel{\boldsymbol{u}_s} \boldsymbol{v}_s\right) = 0 \tag{7a}$$

$$\frac{\partial n_f S_w \rho_w}{\partial t} + \boldsymbol{\nabla} \cdot \left(n_f S_w \rho_w \cancel{\boldsymbol{u}_w} \boldsymbol{v}_w\right) = 0 \tag{7b}$$

$$\frac{\partial n_f S_n \rho_n}{\partial t} + \boldsymbol{\nabla} \cdot \left(n_f S_n \rho_n \cancel{\boldsymbol{u}_n} \boldsymbol{v}_n\right) = 0 \tag{7c}$$

with ρ_π the density and ~~$\boldsymbol{u}_\pi$~~ $\boldsymbol{v}_\pi$ the velocity of phase $\pi = s, w, n$, and n_f the porosity of the porous material, which is assumed to be constant. It is further assumed that the effect of density gradients is negligible. The time derivatives of the density are simplified using the bulk moduli of the solid and fluids as:

$$\frac{1}{\rho_s}\frac{\partial \rho_s}{\partial t} = \frac{1}{1-n_f}\left(\frac{\alpha - n_f}{K_s}\frac{\partial S_w p_w + S_n p_n}{\partial t} - (1-\alpha)\boldsymbol{\nabla} \cdot \cancel{\boldsymbol{u}_s} \boldsymbol{v}_s\right) \tag{8a}$$

$$\frac{1}{\rho_w}\frac{\partial \rho_w}{\partial t} = \frac{1}{K_w}\frac{\partial p_w}{\partial t} \tag{8b}$$

$$\frac{1}{\rho_n}\frac{\partial \rho_n}{\partial t} = \frac{1}{K_n}\frac{\partial p_n}{\partial t} \tag{8c}$$

using the bulk moduli of the solid, wetting phase and non-wetting phase K_s, K_w, and K_n, respectively. By denoting the velocity difference between the solid and wetting phase as ~~$\boldsymbol{q}_w = n_f S_w(\boldsymbol{u}_w - \boldsymbol{u}_s)$~~ $\boldsymbol{q}_w = n_f S_w(\boldsymbol{v}_w - \boldsymbol{v}_s)$ and between the solid and non-wetting phase as ~~$\boldsymbol{q}_n = n_f S_n(\boldsymbol{u}_n - \boldsymbol{u}_s)$~~ $\boldsymbol{q}_n = n_f S_n(\boldsymbol{v}_n - \boldsymbol{v}_s)$, the mass balances of Eq. (7) can be combined with the definitions of the density changes in Eq. (8), resulting in:

$$\frac{1}{M_{ww}}\dot{p}_w + \frac{1}{M_{wn}}\dot{p}_n + \alpha S_w \boldsymbol{\nabla} \cdot \dot{\boldsymbol{u}} + \boldsymbol{\nabla} \cdot \boldsymbol{q}_w = 0 \tag{9a}$$

$$\frac{1}{M_{nn}}\dot{p}_n + \frac{1}{M_{nw}}\dot{p}_w + \alpha S_n \boldsymbol{\nabla} \cdot \dot{\boldsymbol{u}} + \boldsymbol{\nabla} \cdot \boldsymbol{q}_n = 0 \tag{9b}$$

Herein the local pressure capacities are given by:

$$\frac{1}{M_{ww}} = S_w \frac{\alpha - n_f}{K_s}\left(S_w + p_c \frac{\partial S_w}{\partial p_c}\right) - n_f \frac{\partial S_w}{\partial p_c} + \frac{n_f S_w}{K_w} \tag{10a}$$

$$\frac{1}{M_{wn}} = S_w \frac{\alpha - n_f}{K_s}\left(S_n - p_c \frac{\partial S_w}{\partial p_c}\right) + n_f \frac{\partial S_w}{\partial p_c} \tag{10b}$$

$$\frac{1}{M_{nw}} = S_n \frac{\alpha - n_f}{K_s}\left(S_w + p_c \frac{\partial S_w}{\partial p_c}\right) + n_f \frac{\partial S_w}{\partial p_c} \tag{10c}$$

$$\frac{1}{M_{nn}} = S_n \frac{\alpha - n_f}{K_s}\left(S_n - p_c \frac{\partial S_w}{\partial p_c}\right) - n_f \frac{\partial S_w}{\partial p_c} + \frac{n_f S_n}{K_n} \tag{10d}$$

The fluid fluxes inside the poroelastic media are given by Darcy's law:

$$\boldsymbol{q}_w = S_w n_f \left(\boldsymbol{v}_w - \dot{\boldsymbol{u}}\right) = -k_w k_{rw} \boldsymbol{\nabla} p_w \tag{11a}$$

$$\boldsymbol{q}_n = S_n n_f \left(\boldsymbol{v}_n - \dot{\boldsymbol{u}}\right) = -k_n k_{rn} \boldsymbol{\nabla} p_n \tag{11b}$$

with the permeabilities $k_w = k/\mu_w$ and $k_n = k/\mu_n$. k is the intrinsic permeability, and μ_w and μ_n are the viscosities of the wetting and non-wetting phases, respectively. The relative permeabilities, k_{rw} and k_{rn}, are functions of the degree of saturation [17]. Here, we use a relation for a water-oil mixture to describe the relative permeabilities [15]:

$$k_{rw} = S_w^5 \tag{12a}$$

$$k_{rn} = (1 - S_w)^5 \tag{12b}$$

2.2. Fractures

The fracture is modelled using isogeometric interface elements [51, 52]. The degree of saturation inside the fracture is assumed to be equal to that in the surrounding porous medium. An alternative of this assumption would be using a separate relation to relate the wetting and non-wetting phase pressures to the saturations within the fracture. While this may represent the saturation more accurately represent, it would add complexity to the sub-grid model, and has therefore not been used.

The traction at the discontinuity, $\boldsymbol{t}_{\Gamma_d}$, is composed of an effective traction $\boldsymbol{t}_d$ and the pressures acting on the wall:

$$\boldsymbol{t}_{\Gamma_d} = \boldsymbol{t}_d - (S_w p_w + S_n p_n)\,\boldsymbol{n} \tag{13}$$

Since only non-propagating fractures have been simulated, the effective tractions have been assumed to be zero for all fractured elements (no cohesive tractions: $\boldsymbol{t}_d = \boldsymbol{0}$).

~~Interface elements were also inserted in the line which extends from the crack tips.~~ The used spatial discretisation method requires interface elements to be inserted for both the fractured part of the discontinuity, and in the extension of the fracture where the material is intact. While the interface elements which represent the fracture are allowed to open freely, the interface elements not located on the fracture are required to retain a continuous displacement. To prevent these non-fractured interface elements from opening, a linear relation between the traction and the fracture opening height was assumed:

$$\boldsymbol{t}_d = \boldsymbol{D}_d [\![\boldsymbol{u}]\!] \tag{14}$$

with $[\![\boldsymbol{u}]\!]$ the fracture opening height and $\boldsymbol{D}_d$ the interface stiffness matrix given by:

$$\boldsymbol{D}_d = \begin{bmatrix} k_n & 0 \\ 0 & k_s \end{bmatrix} \tag{15}$$

with k_n and k_s (dummy) stiffnesses which are sufficiently large to prevent the fracture from opening. Since these relations are in the local, $(\overline{s}, \overline{n})$, coordinate system, the interface stiffness matrix is rotated using the rotation matrix $\boldsymbol{R}$ to the global coordinate system:

$$\overline{\boldsymbol{D}}_d = \boldsymbol{R}^T \boldsymbol{D}_d \boldsymbol{R} \tag{16}$$

The wetting phase fracture inflow is obtained from the mass conservation of the wetting phase inside the fracture:

$$\frac{\partial v_w}{\partial \overline{s}} - + \frac{\partial w_w}{\partial \overline{n}} = 0 \tag{17}$$

with v_w and w_w the velocity components in the $\overline{s}$ and $\overline{n}$ directions, respectively. This assumes that density gradients are negligible inside the fracture compared to the fluid velocity. This is in contrast to the interior of the porous domain, where due to the lower fluid velocity and the compression by deformations of the solid the density changes are included in Eq. (7). Integrating Eq. (17) over the fracture height results in the jump in fluid velocity:

$$[\![w]\!]_w = w_w\left(\frac{h}{2}\right) - w_w\left(-\frac{h}{2}\right) = -\frac{\partial q_w}{\partial \overline{s}} \tag{18}$$

with the total wetting phase flux inside the fracture defined by:

$$q_w = \int_{-h/2}^{h/2} v_w \mathrm{d}\overline{n} \tag{19}$$

Eq. (18) is used to define the coupling between the interstitial fluid pressures and the fluid flow inside the fracture via [16, 45]:

$$\boldsymbol{n}_{\Gamma_d} \cdot \boldsymbol{q}_w = \frac{1}{2}\left(\llbracket w \rrbracket_w - \llbracket w \rrbracket_{ws}\right) \tag{20}$$

with the inflow due to changes in fracture height and saturation given by:

$$\llbracket w \rrbracket_{ws} = \frac{\partial S_w h}{\partial t} \tag{21}$$

Similarly, for the non-wetting phase:

$$\boldsymbol{n}_{\Gamma_d} \cdot \boldsymbol{q}_n = \frac{1}{2}\left(\llbracket w \rrbracket_n - \llbracket w \rrbracket_{ns}\right) \tag{22}$$

with:

$$\llbracket w \rrbracket_n = w_n\left(\frac{h}{2}\right) - w_n\left(-\frac{h}{2}\right) = -\frac{\partial q_n}{\partial \overline{s}} \tag{23}$$

$$q_n = \int_{-h/2}^{h/2} v_n \mathrm{d}\overline{n} \tag{24}$$

$$\llbracket w \rrbracket_{ns} = \frac{\partial S_n h}{\partial t} \tag{25}$$

Eqs (18) and (23) can be used with different definitions for the fluid velocity profile in the fracture. Next, we will describe velocity profiles for bubbly and separated flows. These will be compared to the cubic law, as this is often combined with an empirical relative permeability function to describe the fluid flow inside fractures. While we will compare these three models by simulating the same case for all models, the choice of model should depend on which flow regime the flow is expected to occur. Experiments using water and air in smooth, non-porous, channels indicate that the bubbly flow model is appropriate for the slow-moving fluids [23, 53]. However, separated flow in fractures has been observed for gas/water and oil/water mixtures [54, 55], and has been used for the simulation of non-porous fractures [56, 26]. It is therefore important to note that while we will show that these models will provide different results for the same case, the separated and bubbly flow models do represent different flow regimes and the actual choice of model should be motivated by the physics of the problem at hand.

2.2.1. Cubic law

The cubic law describes the fluid flux of phase π inside the fracture as:

$$q_\pi = -\frac{k_{d\pi} h^3}{12\mu_\pi}\frac{\partial p_\pi}{\partial \overline{s}} \tag{26}$$

with $k_{d\pi}$ the relative permeability of the wetting and non-wetting phases inside the fracture. Similar to the relative permeability inside the porous media, we will use a relation from [15] to describe the relative fracture permeability as:

$$k_{dw} = S_w^3 \tag{27a}$$

$$k_{dn} = S_n^3 \tag{27b}$$

Using the fluid flux of Eq. (26) and the definitions for the relative permeability, Eqs (20) and (21) can be exploited to derive an expression for the fracture outflow:

$$2\boldsymbol{n}_{\Gamma_d} \cdot \boldsymbol{q}_w = \frac{S_w^3 h^3}{12\mu_w}\frac{\partial^2 p_w}{\partial \overline{s}^2} + \frac{h^2 S_w^3}{4\mu_w}\frac{\partial p_w}{\partial \overline{s}}\frac{\partial h}{\partial \overline{s}} + \frac{S_w^2 h^3}{4\mu_w}\frac{\partial S_w}{\partial p_c}\left(\frac{\partial p_n}{\partial \overline{s}} - \frac{\partial p_w}{\partial \overline{s}}\right)\frac{\partial p_w}{\partial \overline{s}} - S_w \dot{h} - h\dot{S}_w \tag{28a}$$

$$2\boldsymbol{n}_{\Gamma_d} \cdot \boldsymbol{q}_n = \frac{S_n^3 h^3}{12\mu_n}\frac{\partial^2 p_n}{\partial \overline{s}^2} + \frac{h^2 S_n^3}{4\mu_n}\frac{\partial p_n}{\partial \overline{s}}\frac{\partial h}{\partial \overline{s}} - \frac{S_n^2 h^3}{4\mu_n}\frac{\partial S_w}{\partial p_c}\left(\frac{\partial p_n}{\partial \overline{s}} - \frac{\partial p_w}{\partial \overline{s}}\right)\frac{\partial p_n}{\partial \overline{s}} - S_n \dot{h} - h\dot{S}_n \tag{28b}$$

2.2.2. Volume averaged bubbly flow

To describe the flow inside the fracture as a well-mixed flow, we obtain the volume-averaged viscosity as:

$$\overline{\mu} = S_w \mu_w + S_n \mu_n \tag{29}$$

Using this viscosity the velocity of the mixture is obtained as:

$$0 = -\left(S_w \frac{\partial p_w}{\partial \overline{s}} + S_n \frac{\partial p_n}{\partial \overline{s}}\right) + \frac{\partial}{\partial \overline{n}}\left(\overline{\mu}\frac{\partial \overline{v}}{\partial \overline{n}}\right) \tag{30}$$

Using Eq. (30) with a no slip boundary condition at the walls of the fracture results in the velocity profile, from which the velocities in the wetting and the non-wetting phases are obtained:

$$v_w = S_w \overline{v} = \frac{1}{2}\frac{S_w}{S_w\mu_w + S_n\mu_n}\left(S_w \frac{\partial p_w}{\partial \overline{s}} + S_n \frac{\partial p_n}{\partial \overline{s}}\right)\left(\overline{n}^2 - \left(\frac{h}{2}\right)^2\right) \quad \text{for} \quad -\frac{h}{2} < \overline{n} < \frac{h}{2} \tag{31a}$$

$$v_n = S_n \overline{v} = \frac{1}{2}\frac{S_n}{S_w\mu_w + S_n\mu_n}\left(S_w \frac{\partial p_w}{\partial \overline{s}} + S_n \frac{\partial p_n}{\partial \overline{s}}\right)\left(\overline{n}^2 - \left(\frac{h}{2}\right)^2\right) \quad \text{for} \quad -\frac{h}{2} < \overline{n} < \frac{h}{2} \tag{31b}$$

From Eq. (19) we subsequently obtain the total flux as:

$$q_w = -\frac{S_w h^3}{12\left(S_w\mu_w + S_n\mu_n\right)}\left(S_w \frac{\partial p_w}{\partial \overline{s}} + S_n \frac{\partial p_n}{\partial \overline{s}}\right) \tag{32a}$$

$$q_n = -\frac{S_n h^3}{12\left(S_w\mu_w + S_n\mu_n\right)}\left(S_w \frac{\partial p_w}{\partial \overline{s}} + S_n \frac{\partial p_n}{\partial \overline{s}}\right) \tag{32b}$$

Different from the fluxe~~d~~ s in Eq. (26) obtained for the cubic law, the fluid transported inside the fracture is influenced not only by the pressure gradient of the phase itself, but also by the pressure gradient of the other phase. This can be viewed as a high pressure gradient phase dragging the low pressure gradient phase along. This effect increases the flux of the low-gradient phase and decreases the flux of the high-gradient phase. The fracture inflow velocities are obtained from Eq. (20):

$$\begin{aligned}2\boldsymbol{n}_{\Gamma_d}\cdot\boldsymbol{q}_w = {} & \frac{S_w h^3}{12\left(S_w\mu_w + S_n\mu_n\right)}\left(S_w \frac{\partial^2 p_w}{\partial \overline{s}^2} + S_n \frac{\partial^2 p_w}{\partial \overline{s}^2} + \left(\frac{\partial p_w}{\partial \overline{s}} - \frac{\partial p_n}{\partial \overline{s}}\right)\frac{\partial S_w}{\partial p_c}\left(\frac{\partial p_n}{\partial \overline{s}} - \frac{\partial p_w}{\partial \overline{s}}\right)\right) \\ & + \frac{h^3}{12}\left(S_w \frac{\partial p_w}{\partial \overline{s}} + S_n \frac{\partial p_n}{\partial \overline{s}}\right)\left(\left(S_w\mu_w + S_n\mu_n\right)^{-1} - S_w\left(S_w\mu_w + S_n\mu_n\right)^{-2}\left(\mu_w - \mu_n\right)\right)\frac{\partial S_w}{\partial p_c}\left(\frac{\partial p_n}{\partial \overline{s}} - \frac{\partial p_w}{\partial \overline{s}}\right) \\ & + \frac{S_w h^2}{4\left(S_w\mu_w + S_n\mu_n\right)}\left(S_w \frac{\partial p_w}{\partial \overline{s}} + S_n \frac{\partial p_n}{\partial \overline{s}}\right)\frac{\partial h}{\partial \overline{s}} - S_w\dot{h} - h\dot{S}_w\end{aligned} \tag{33a}$$

$$\begin{aligned}2\boldsymbol{n}_{\Gamma_d}\cdot\boldsymbol{q}_n = {} & \frac{S_n h^3}{12\left(S_w\mu_w + S_n\mu_n\right)}\left(S_w \frac{\partial^2 p_w}{\partial \overline{s}^2} + S_n \frac{\partial^2 p_w}{\partial \overline{s}^2} + \left(\frac{\partial p_w}{\partial \overline{s}} - \frac{\partial p_n}{\partial \overline{s}}\right)\frac{\partial S_w}{\partial p_c}\left(\frac{\partial p_n}{\partial \overline{s}} - \frac{\partial p_w}{\partial \overline{s}}\right)\right) \\ & + \frac{h^3}{12}\left(S_w \frac{\partial p_w}{\partial \overline{s}} + S_n \frac{\partial p_n}{\partial \overline{s}}\right)\left(-\left(S_w\mu_w + S_n\mu_n\right)^{-1} - S_n\left(S_w\mu_w + S_n\mu_n\right)^{-2}\left(\mu_w - \mu_n\right)\right)\frac{\partial S_w}{\partial p_c}\left(\frac{\partial p_n}{\partial \overline{s}} - \frac{\partial p_w}{\partial \overline{s}}\right) \\ & + \frac{S_n h^2}{4\left(S_w\mu_w + S_n\mu_n\right)}\left(S_w \frac{\partial p_w}{\partial \overline{s}} + S_n \frac{\partial p_n}{\partial \overline{s}}\right)\frac{\partial h}{\partial \overline{s}} - S_n\dot{h} - h\dot{S}_n\end{aligned} \tag{33b}$$

2.2.3. Separated flow

For the separated flow profile, the wetting phase is assumed to be the outer phase with layers of height $\frac{1}{2}h_w = \frac{1}{2}S_w h$ at both the top and the bottom of the fracture, as shown in Figure 1. The non-wetting phase is the inner phase with a total height of $h_n = S_n h$. The fluid velocity of the wetting and non-wetting phases are described by Stokes' equation for the individual phases:

$$0 = -\frac{\partial p_w}{\partial \overline{s}} + \frac{\partial}{\partial \overline{n}}\left(\mu_w \frac{\partial v_w}{\partial \overline{n}}\right) \qquad \text{for} \qquad \frac{S_n h}{2} < |\overline{n}| < \frac{h}{2} \tag{34a}$$

$$0 = -\frac{\partial p_n}{\partial \overline{s}} + \frac{\partial}{\partial \overline{n}}\left(\mu_n \frac{\partial v_n}{\partial \overline{n}}\right) \qquad \text{for} \qquad -\frac{S_n h}{2} < \overline{n} < \frac{S_n h}{2} \tag{34b}$$

with the boundary conditions:

$$v_w\left(-\frac{h}{2}\right) = v_w\left(\frac{h}{2}\right) = 0 \tag{35a}$$

$$v_w\left(\frac{S_n h}{2}\right) = v_n\left(\frac{S_n h}{2}\right) \tag{35b}$$

$$\mu_w \frac{\partial v_w}{\partial \overline{n}}\bigg|_{\frac{S_n h}{2}} = \mu_n \frac{\partial v_n}{\partial \overline{n}}\bigg|_{\frac{S_n h}{2}} \tag{35c}$$

$$\frac{\partial v_n}{\partial \overline{n}}\bigg|_0 = 0 \tag{35d}$$

Use of Eqs (34a)-(35d) results in expressions for the velocities in each of the phases:

$$v_w = \begin{cases} \frac{1}{2\mu_w}\frac{\partial p_w}{\partial \overline{s}}\left(|\overline{n}|^2 - \left(\frac{h}{2}\right)^2\right) + \frac{S_n h}{2\mu_w}\frac{\partial p_c}{\partial \overline{n}}\left(|\overline{n}| - \frac{h}{2}\right) & \text{for} \quad \frac{S_n h}{2} < |\overline{n}| < \frac{h}{2} \\ 0 & \text{for} \quad -\frac{S_n h}{2} < \overline{n} < \frac{S_n h}{2} \end{cases} \tag{36a}$$

$$v_n = \begin{cases} 0 & \text{for} \quad \frac{S_n h}{2} < |\overline{n}| < \frac{h}{2} \\ \frac{1}{2\mu_n}\frac{\partial p_n}{\partial \overline{s}}\left(|n|^2 - \left(\frac{Snh}{2}\right)^2\right) + \frac{1}{2\mu_w}\frac{\partial p_w}{\partial \overline{s}}\left(\left(\frac{S_n h}{2}\right)^2 - \left(\frac{h}{2}\right)^2\right) & \\ \qquad + \frac{1}{\mu_w}\frac{\partial p_c}{\partial \overline{s}}\left(\left(\frac{S_n h}{2}\right)^2 - S_n\left(\frac{h}{2}\right)^2\right) & \text{for} \quad -\frac{S_n h}{2} < \overline{n} < \frac{S_n h}{2} \end{cases} \tag{36b}$$

Similar to the model for bubbly flow, these velocities depend on the pressure gradients of the phase itself, but also on that of the other phase. These velocity profiles result in the fracture fluid transport:

$$q_w = -\frac{h^3}{\mu_w}\frac{\partial p_w}{\partial \overline{s}}\left(\frac{1}{12} - \frac{1}{8}S_n + \frac{1}{24}S_n^3\right) - \frac{h^3}{\mu_w}\frac{\partial p_c}{\partial \overline{s}}\left(\frac{1}{8}S_n - \frac{1}{4}S_n^2 + \frac{1}{8}S_n^3\right) \tag{37a}$$

$$q_n = -\frac{S_n^3 h^3}{12\mu_n}\frac{\partial p_n}{\partial \overline{s}} - \frac{h^3}{\mu_w}\frac{\partial p_w}{\partial \overline{s}}\left(\frac{1}{8}S_n - \frac{1}{8}S_n^3\right) - \frac{h^3}{\mu_w}\frac{\partial p_c}{\partial \overline{s}}\left(\frac{1}{4}S_n^2 - \frac{1}{4}S_n^3\right) \tag{37b}$$

Substituting Eq. (37a) in the definition for the fracture inflow velocity, Eq. (20), results in:

$$\begin{aligned} 2\boldsymbol{n}_{\Gamma_d} \cdot \boldsymbol{q}_w = {} & \frac{h^3}{\mu_w}\frac{\partial^2 p_w}{\partial \overline{s}^2}\left(\frac{1}{12} - \frac{1}{8}S_n + \frac{1}{24}S_n^3\right) + \frac{h^2}{\mu_w}\frac{\partial p_w}{\partial \overline{s}}\frac{\partial h}{\partial \overline{s}}\left(\frac{1}{4}h^2 - \frac{3}{8}S_n h^2 + \frac{1}{8}S_n^3 h^2\right) \\ & + \frac{h^3}{\mu_w}\frac{\partial p_w}{\partial \overline{s}}\frac{\partial S_w}{\partial p_c}\left(\frac{\partial p_n}{\partial \overline{s}} - \frac{\partial p_w}{\partial \overline{s}}\right)\left(\frac{1}{8} - \frac{1}{8}S_n^2\right) + \frac{h^3}{\mu_w}\left(\frac{\partial^2 p_n}{\partial \overline{s}^2} - \frac{\partial^2 p_w}{\partial \overline{s}^2}\right)\left(\frac{1}{8}S_n - \frac{1}{4}S_n^2 + \frac{1}{8}S_n^3\right) \\ & + \frac{h^2}{\mu_w}\frac{\partial p_c}{\partial \overline{s}}\frac{\partial h}{\partial \overline{s}}\left(\frac{3}{8}S_n - \frac{3}{4}S_n^2 + \frac{3}{8}S_n^3\right) + \frac{h^3}{\mu_w}\frac{\partial p_c}{\partial \overline{s}}\frac{\partial p_n}{\partial \overline{s}} - \frac{\partial p_w}{\partial \overline{s}}\left(-\frac{1}{8} + \frac{1}{2}S_n - \frac{3}{8}S_n^2\right) - S_w\dot{h} - h\dot{S}_w \end{aligned} \tag{38}$$

In a similar way, the fracture inflow for the non-wetting phase is obtained from Eqs (20) and (37b):

$$\begin{aligned}2\boldsymbol{n}_{\Gamma_d}\cdot\boldsymbol{q}_n = {} & \frac{S_n^3 h^3}{12\mu_n}\frac{\partial p_n^2}{\partial \overline{s}^2} + \frac{h^2 S_n^3}{4\mu_n}\frac{\partial h}{\partial \overline{s}}\frac{\partial p_n}{\partial \overline{s}} - \frac{h^3 S_n^2}{4\mu_n}\frac{\partial p_n}{\partial \overline{s}}\frac{\partial S_w}{\partial p_c}\left(\frac{\partial p_n}{\partial \overline{s}} - \frac{\partial p_w}{\partial \overline{s}}\right) \\ & + \frac{h^3}{\mu_w}\frac{\partial^2 p_w}{\partial \overline{s}^2}\left(\frac{1}{8}S_n - \frac{1}{8}S_n^3\right) + \frac{h^2}{\mu_w}\frac{\partial p_w}{\partial \overline{s}}\frac{\partial h}{\partial \overline{s}}\left(\frac{3}{8}S_n - \frac{3}{8}S_n^3\right) + \frac{h^3}{\mu_w}\frac{\partial p_w}{\partial \overline{s}}\frac{\partial S_w}{\partial p_c}\left(\frac{\partial p_n}{\partial \overline{s}} - \frac{\partial p_w}{\partial \overline{s}}\right)\left(-\frac{1}{8} + \frac{3}{8}S_n^2\right) \\ & + \frac{h^3}{\mu_w}\left(\frac{\partial^2 p_n}{\partial \overline{s}^2} - \frac{\partial^2 p_w}{\partial \overline{s}^2}\right)\left(\frac{1}{4}S_n^2 - \frac{1}{4}S_n^3\right) + \frac{h^2}{\mu_w}\frac{\partial p_c}{\partial \overline{s}}\frac{\partial h}{\partial \overline{s}}\left(\frac{3}{4}S_n^2 - \frac{3}{4}S_n^3\right) \\ & + \frac{h^3}{\mu_w}\frac{\partial p_c}{\partial \overline{s}}\frac{\partial S_w}{\partial p_c}\left(\frac{\partial p_n}{\partial \overline{s}} - \frac{\partial p_w}{\partial \overline{s}}\right)\left(-\frac{1}{2}S_n + \frac{3}{4}S_n^2\right) - S_n\dot{h} - h\dot{S}_n \end{aligned} \quad (39)$$

3. Discretisation

The weak form of the momentum balance is obtained from Eqs (3)-(6) by multiplying them with the test function $\boldsymbol{\eta}$ and using the divergence theorem. This leads to:

$$\int_\Omega \boldsymbol{\nabla}\boldsymbol{\eta} : (\boldsymbol{\sigma}_s - \alpha S_w p_w \boldsymbol{I} - \alpha S_n p_n \boldsymbol{I})\,\mathrm{d}\Omega - \int_{\Gamma_d} \boldsymbol{\eta}\cdot(\boldsymbol{t}_d - \boldsymbol{n}_d(S_w p_w + S_n p_n))\,\mathrm{d}\Gamma = \int_\Gamma \boldsymbol{\eta}\cdot\bar{\boldsymbol{t}}\mathrm{d}\Gamma \quad (40)$$

with Ω the domain representing the interior, Γ the external boundaries, and Γ_d the discontinuity. The weak forms of the mass balances, Eqs (9a) and (9b), are obtained by multiplying them with the test functions ζ and ξ, and using the divergence theorem on the fluid flux and fracture inflow terms. This results in:

$$\int_\Omega \zeta\frac{1}{M_{ww}}\dot{p}_w + \zeta\frac{1}{M_{wn}}\dot{p}_n + \alpha S_w \zeta \boldsymbol{\nabla}\cdot\dot{\boldsymbol{u}} + k_w k_{rw}\boldsymbol{\nabla}\zeta\cdot\boldsymbol{\nabla}\boldsymbol{p}_w \mathrm{d}\Omega - \int_{\Gamma_d}\frac{\partial\zeta}{\partial\overline{s}}q_w + \zeta\frac{\partial S_w h}{\partial t}\mathrm{d}\Gamma_d = -\int_\Gamma \zeta\overline{q}_w \mathrm{d}\Gamma - \int_{\partial\Gamma_d}\zeta Q_w \mathrm{d}\partial\Gamma \quad (41)$$

$$\int_\Omega \xi\frac{1}{M_{nw}}\dot{p}_w + \xi\frac{1}{M_{nn}}\dot{p}_n + \alpha S_n \xi \boldsymbol{\nabla}\cdot\dot{\boldsymbol{u}} + k_n k_{rn}\boldsymbol{\nabla}\xi\cdot\boldsymbol{\nabla}\boldsymbol{p}_n \mathrm{d}\Omega - \int_{\Gamma_d}\frac{\partial\xi}{\partial\overline{s}}q_n + \xi\frac{\partial S_n h}{\partial t}\mathrm{d}\Gamma_d = -\int_\Gamma \xi\overline{q}_n \mathrm{d}\Gamma - \int_{\partial\Gamma_d}\xi Q_n \mathrm{d}\partial\Gamma \quad (42)$$

with q_w and q_n depending on the model for the flow inside the fracture, and Q_w and Q_n the fracture outflow at the edges of the discontinuity ($\partial\Gamma_d$), assumed to be zero.

Since the velocity inside the porous medium depends on the pressure gradient, and the fracture inflow depends on second gradients, a C^2 inter-element continuity is required to obtain continuous fracture inflows [45] and smooth interstitial fluid velocities [57]. In order to achieve this inter-element continuity, Non-Uniform Rational B-Splines (NURBS) are used to discretise the weak forms [58]. To use these NURBS in a similar manner as traditional Lagrangian finite elements, Bézier extraction is employed to describe the continuous NURBS as a combination of Bernstein polynomials [59], which allows the system matrices and internal force vectors to be calculated on a per-element basis. Similarly, Bézier extracted interface elements are used to discretise the discontinuity [51, 52].

The weak forms of Eqs (40)-(42) have been discretised using cubic Bézier extracted NURBS for the shape functions $\boldsymbol{N}_w$ and $\boldsymbol{N}_n$ for the wetting and non-wetting pressures, respectively. In order to prevent spurious oscillations the inf-sup requirements has to be fulfilled [60]. Therefore, the solid displacements ha~~s~~ ve been discretised using quartic NURBS $\boldsymbol{N}_s$. This results in the displacements and pressures being discretised as:

$$\boldsymbol{u} = \sum_{e=1}^{n_{el}} \boldsymbol{N}_s \boldsymbol{u}^{el} \quad (43)$$

$$p_w = \sum_{e=1}^{n_{el}} \boldsymbol{N}_w \boldsymbol{p}_w^{el} \quad (44)$$

$$p_n = \sum_{e=1}^{n_{el}} \boldsymbol{N}_n \boldsymbol{p}_n^{el} \quad (45)$$

The strain-nodal displacement matrix $\boldsymbol{B}$ is used to map the displacements to the strains on an element level:

$$\boldsymbol{\epsilon}^{el} = \boldsymbol{B}\boldsymbol{u}^{el} \tag{46}$$

Use of the interpolations for the displacements and for the pressures, and the $\boldsymbol{B}$ matrix to discretise the weak form of the momentum balance, Eq. (40), results in:

$$\boldsymbol{f}_{ext} - \boldsymbol{f}_{int} - \boldsymbol{f}_d = 0 \tag{47}$$

with the external force $\boldsymbol{f}_{ext}$ defined in a standard manner as:

$$\boldsymbol{f}_{ext} = \int_{\Gamma_t} \boldsymbol{N}_s^T \bar{\boldsymbol{t}} \mathrm{d}\Gamma \tag{48}$$

The internal force which results from the bulk, $\boldsymbol{f}_{int}$, is given by:

$$\boldsymbol{f}_{int} = \int_\Omega \boldsymbol{B}^T \boldsymbol{\sigma}_s \,\mathrm{d}\Omega - \int_\Omega \alpha S_w \boldsymbol{B}^T \boldsymbol{m} \boldsymbol{N}_w \boldsymbol{p}_w^{el} \,\mathrm{d}\Omega - \int_\Omega \alpha S_n \boldsymbol{B}^T \boldsymbol{m} \boldsymbol{N}_n \boldsymbol{p}_n^{el} \,\mathrm{d}\Omega \tag{49}$$

with $\boldsymbol{m} = [1\ 1\ 0]^T$. The degrees of saturation S_w and S_n are calculated in the integration points using Eq. (2). The ~~strong~~ dependence of this saturation on the wetting and non-wetting phase pressures results in a non-linear dependence on the pressures.

The fracture is discretised using interface elements and a mapping is introduced which relates the displacements at the interface Γ_d to the jump in the displacement at the interface:

$$[\![\boldsymbol{u}]\!]^{el} = \boldsymbol{N}_d \boldsymbol{u}^{el} \qquad \boldsymbol{N}_d = \begin{bmatrix} -\boldsymbol{N}_s & \boldsymbol{0} \\ \boldsymbol{0} & \boldsymbol{N}_s \end{bmatrix} \tag{50}$$

Use of this identity at the internal discontinuity Γ_d allows the term in the momentum balance which pertains to this discontinuity to be written as:

$$\boldsymbol{f}_d = \int_{\Gamma_d} \boldsymbol{N}_d^T \boldsymbol{R}^T \boldsymbol{D}_d \boldsymbol{R} \boldsymbol{N}_d \boldsymbol{u}^{el} \,\mathrm{d}\Gamma - \int_{\Gamma_d} S_w \boldsymbol{N}_d^T \boldsymbol{n}_{\Gamma_d} \boldsymbol{N}_w \boldsymbol{p}_w^{el} \,\mathrm{d}\Gamma - \int_{\Gamma_d} S_n \boldsymbol{N}_d^T \boldsymbol{n}_{\Gamma_d} \boldsymbol{N}_n \boldsymbol{p}_n^{el} \,\mathrm{d}\Gamma \tag{51}$$

The weak forms of mass conservation for the wetting phase mass, Eq. (41), and for the non-wetting phase, Eq. (42), are discretised using Equations (43)–(45). The temporal discretisation is achieved using a backward finite difference scheme, resulting in:

$$\boldsymbol{q}_{w,ext} - \boldsymbol{q}_{w,int} - \boldsymbol{q}_{w,d} = \boldsymbol{0} \tag{52}$$

$$\boldsymbol{q}_{n,ext} - \boldsymbol{q}_{n,int} - \boldsymbol{q}_{n,d} = \boldsymbol{0} \tag{53}$$

with the external fluxes defined as:

$$\boldsymbol{q}_{w,ext} = \Delta t \int_\Gamma \boldsymbol{N}_w^T \bar{q}_w \mathrm{d}\Gamma + \Delta t \int_{\partial\Gamma_d} \boldsymbol{N}_w^T Q_w \mathrm{d}\partial\Gamma \tag{54}$$

$$\boldsymbol{q}_{n,ext} = \Delta t \int_\Gamma \boldsymbol{N}_n^T \bar{q}_n \mathrm{d}\Gamma + \Delta t \int_{\partial\Gamma_d} \boldsymbol{N}_n^T Q_n \mathrm{d}\partial\Gamma \tag{55}$$

and the internal fluxes defined as:

$$\begin{aligned} \boldsymbol{q}_{w,int} = & -\int_\Omega \alpha S_w \boldsymbol{N}_w^T \boldsymbol{m}^T \boldsymbol{B} \left(\boldsymbol{u}^{t+\Delta t} - \boldsymbol{u}^t\right) \mathrm{d}\Omega - \int_\Omega \Delta t k_w k_{rw} (\boldsymbol{\nabla} \boldsymbol{N}_w)^T \boldsymbol{\nabla} \boldsymbol{N}_w \boldsymbol{p}_w^{t+\Delta t} \mathrm{d}\Omega \\ & - \int_\Omega \frac{1}{M}_{ww} \boldsymbol{N}_w^T \boldsymbol{N}_w \left(\boldsymbol{p}_w^{t+\Delta t} - \boldsymbol{p}_w^t\right) \mathrm{d}\Omega - \int_\Omega \frac{1}{M}_{wn} \boldsymbol{N}_w^T \boldsymbol{N}_n \left(\boldsymbol{p}_n^{t+\Delta t} - \boldsymbol{p}_n^t\right) \mathrm{d}\Omega \end{aligned} \tag{56}$$

$$
\begin{aligned}
\boldsymbol{q}_{n,int} = &-\int_\Omega \alpha S_n \boldsymbol{N}_n^T \boldsymbol{m}^T \boldsymbol{B}\left(\boldsymbol{u}^{t+\Delta t} - \boldsymbol{u}^t\right) \mathrm{d}\Omega - \int_\Omega \Delta t k_n k_{rn} (\boldsymbol{\nabla}\boldsymbol{N}_n)^T \boldsymbol{\nabla}\boldsymbol{N}_n \boldsymbol{p}_n^{t+\Delta t} \mathrm{d}\Omega \\
&- \int_\Omega \frac{1}{M}_{nw} \boldsymbol{N}_n^T \boldsymbol{N}_w \left(\boldsymbol{p}_w^{t+\Delta t} - \boldsymbol{p}_w^t\right) \mathrm{d}\Omega - \int_\Omega \frac{1}{M}_{nn} \boldsymbol{N}_n^T \boldsymbol{N}_n \left(\boldsymbol{p}_n^{t+\Delta t} - \boldsymbol{p}_n^t\right) \mathrm{d}\Omega
\end{aligned}
\tag{57}
$$

The fluxes due to the discontinuity are split into two parts: The fluid absorbed and released due to the fracture opening, which is independent of the fracture flow model used, and the pressure-driven flow inside the fracture, which depends on the flow model used.

$$
\boldsymbol{q}_{\pi,d} = \boldsymbol{q}_{\pi,dh} + \boldsymbol{q}_{\pi,dp} \tag{58}
$$

with the fluid flux due to height and saturation changes discretised as:

$$
\boldsymbol{q}_{w,dh} = -\int_{\Gamma_d} S_w \boldsymbol{N}_w^T \boldsymbol{n}_{\Gamma_d}^T \boldsymbol{N}_d \left(\boldsymbol{u}^{t+\Delta t} - \boldsymbol{u}^t\right) + \left(S_w^{t+\Delta t} - S_w^t\right) \boldsymbol{N}_w^T \boldsymbol{n}_{\Gamma_d}^T \boldsymbol{N}_d \boldsymbol{u}^{t+\Delta t} \mathrm{d}\Gamma \tag{59}
$$

$$
\boldsymbol{q}_{n,dh} = -\int_{\Gamma_d} S_n \boldsymbol{N}_n^T \boldsymbol{n}_{\Gamma_d}^T \boldsymbol{N}_d \left(\boldsymbol{u}^{t+\Delta t} - \boldsymbol{u}^t\right) + \left(S_n^{t+\Delta t} - S_n^t\right) \boldsymbol{N}_n^T \boldsymbol{n}_{\Gamma_d}^T \boldsymbol{N}_d \boldsymbol{u}^{t+\Delta t} \mathrm{d}\Gamma \tag{60}
$$

For the cubic-law flow model (Eq. (26), using the relative permeabilities from Eq. (27)), the discretised form of the fluid flux in the fracture due to the pressure-driven flow is given by:

$$
\boldsymbol{q}_{w,dp}^{cubic} = -\int_{\Gamma_d} \frac{\Delta t S_w^3}{12\mu_w} (\boldsymbol{\nabla}\boldsymbol{N}_w)^T \left(\boldsymbol{n}_{\Gamma_d}^T \boldsymbol{N}_d \boldsymbol{u}^{t+\Delta t}\right)^3 \boldsymbol{\nabla}\boldsymbol{N}_w \boldsymbol{P}_w^{t+\Delta t} \mathrm{d}\Gamma \tag{61}
$$

$$
\boldsymbol{q}_{n,dp}^{cubic} = -\int_{\Gamma_d} \frac{\Delta t S_n^3}{12\mu_n} (\boldsymbol{\nabla}\boldsymbol{N}_n)^T \left(\boldsymbol{n}_{\Gamma_d}^T \boldsymbol{N}_d \boldsymbol{u}^{t+\Delta t}\right)^3 \boldsymbol{\nabla}\boldsymbol{N}_n \boldsymbol{P}_n^{t+\Delta t} \mathrm{d}\Gamma \tag{62}
$$

while for the volume-averaged bubbly flow model we have:

$$
\boldsymbol{q}_{w,dp}^{bubbly} = -\int_{\Gamma_d} \frac{\Delta t S_w}{12\left(S_w \mu_w + S_n \mu_n\right)} (\boldsymbol{\nabla}\boldsymbol{N}_w)^T \left(\boldsymbol{n}_{\Gamma_d}^T \boldsymbol{N}_d \boldsymbol{u}^{t+\Delta t}\right)^3 \left(S_w \boldsymbol{\nabla}\boldsymbol{N}_w \boldsymbol{p}_w^{t+\Delta t} + S_n \boldsymbol{\nabla}\boldsymbol{N}_n \boldsymbol{p}_n^{t+\Delta t}\right) \mathrm{d}\Gamma \tag{63}
$$

$$
\boldsymbol{q}_{n,dp}^{bubbly} = -\int_{\Gamma_d} \frac{\Delta t S_n}{12\left(S_w \mu_w + S_n \mu_n\right)} (\boldsymbol{\nabla}\boldsymbol{N}_w)^T \left(\boldsymbol{n}_{\Gamma_d}^T \boldsymbol{N}_d \boldsymbol{u}^{t+\Delta t}\right)^3 \left(S_w \boldsymbol{\nabla}\boldsymbol{N}_w \boldsymbol{p}_w^{t+\Delta t} + S_n \boldsymbol{\nabla}\boldsymbol{N}_n \boldsymbol{p}_n^{t+\Delta t}\right) \mathrm{d}\Gamma \tag{64}
$$

and in the case of the separated flow model:

$$
\begin{aligned}
\boldsymbol{q}_{w,dp}^{separated} = -\int_{\Gamma_d} \frac{\Delta t}{\mu_w} (\boldsymbol{\nabla}\boldsymbol{N}_w)^T \left(\boldsymbol{n}_{\Gamma_d}^T \boldsymbol{N}_d \boldsymbol{u}^{t+\Delta t}\right)^3 \Bigg(& \boldsymbol{\nabla}\boldsymbol{N}_w \boldsymbol{p}_w^{t+\Delta t} \left(\frac{1}{12} - \frac{1}{8} S_n + \frac{1}{24} S_n^3\right) \\
&+ \left(\boldsymbol{\nabla}\boldsymbol{N}_n \boldsymbol{p}_n^{t+\Delta t} - \boldsymbol{\nabla}\boldsymbol{N}_w \boldsymbol{p}_w^{t+\Delta t}\right) \left(\frac{1}{8} S_n - \frac{1}{4} S_n^2 + \frac{1}{8} S_n^3\right)\Bigg) \mathrm{d}\Gamma
\end{aligned}
\tag{65}
$$

$$
\begin{aligned}
\boldsymbol{q}_{n,dp}^{separated} = -\int_{\Gamma_d} \Delta t (\boldsymbol{\nabla}\boldsymbol{N}_n)^T \left(\boldsymbol{n}_{\Gamma_d} \boldsymbol{N}_d \boldsymbol{u}^{t+\Delta t}\right)^3 \Bigg(& \frac{1}{12\mu_n} S_n^3 \boldsymbol{\nabla}\boldsymbol{N}_n \boldsymbol{p}_n^{t+\Delta t} + \frac{1}{8\mu_w} \boldsymbol{\nabla}\boldsymbol{N}_w \boldsymbol{p}_w^{t+\Delta t} \left(S_n - S_n^3\right) \\
&+ \frac{1}{4\mu_w} \left(\boldsymbol{\nabla}\boldsymbol{N}_n \boldsymbol{p}_n^{t+\Delta t} - \boldsymbol{\nabla}\boldsymbol{N}_w \boldsymbol{p}_w^{t+\Delta t}\right) \left(S_n^2 - S_n^3\right)\Bigg) \mathrm{d}\Gamma
\end{aligned}
\tag{66}
$$

Significant pressure oscillations were observed around the phase interface due to the presence of strong gradients, as shown in Figure 2 for the parameters and geometry (excluding the discontinuity) that will be given in detail in the next section. Since the fracture inflow models are dependent on pressure gradients, a stabilisation scheme needs to be applied to prevent these oscillations, and to obtain reasonable results from the fracture inflow models. While many stabilisation methods exist, for instance multi-scale stabilisation [61, 62, 63] and Galerkin least-squares methods [64, 65], a scheme was used based on the observation that

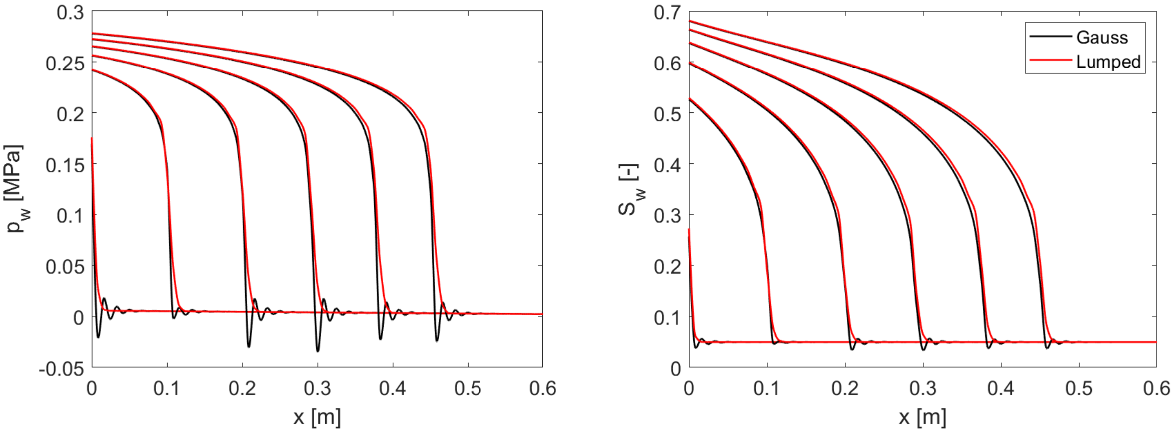

(a)

(b)

Figure 2: Pressure and degree of saturation for the wetting phase for a non-fractured domain using Gauss integration and lumped integration of the pressure capacity terms (profiles at different times).

lumped pressure capacity matrices prevent such oscillations [66]. Applying this scheme to multiphase flows results in the pressure capacity terms given in Eqs (56) and (57), and replace the integral over the domain by a sum over all control points:

$$\int_\Omega \frac{1}{M_{ww}} \boldsymbol{N}_w^T \boldsymbol{N}_w \left(\boldsymbol{p}_w^{t+\Delta t} - \boldsymbol{p}_w^t\right) \mathrm{d}\Omega = \sum_{cp=1}^{n_{cps}} C_{ww} \left(\boldsymbol{p}_{w,cp}^{t+\Delta t} - \boldsymbol{p}_{w,cp}^t\right) \tag{67}$$

The representative pressure capacity is determined by integrating the shape function associated with the control-point (using a standard Gauss integration scheme):

$$C_{ww} = \int_\Omega \frac{1}{M_{ww}} \boldsymbol{N}_{cp} d\Omega \tag{68}$$

with M_{ww} determined at the integration points and $\boldsymbol{N}_{cp}$ the interpolant corresponding to the control point. It therefore depends not only on the pressures in the control point which are integrated with lumped integration, but also on all other control points with non-zero shape functions in the integration point. The result of applying this integration scheme is shown in Figure 2. It is noted that this lumped integration scheme is needed due to the use of NURBS, and a similar lumped pressure capacity would have been achieved using a standard Newton-Cotes integration rule for standard Lagrangian finite elements.

The discretised equations described in this section have been implemented using a Newton-Raphson scheme described in Appendix A. Due to the use of consistently linearised tangential stiffness matrices, quadratic convergence was obtained in all cases.

4. Comparison of subgrid models

To compare the effect of the fracture flow model on the resulting pressures and degrees of saturation, a boundary value problem has been solved which contains a single horizontal fracture. The problem is shown in Figure 3 and contains a single fracture with a length of 0.6 m in a 1 m × 0.2 m porous medium. The bottom of the domain is constrained in the vertical direction, and the left edge is constrained in the horizontal direction.

The simulation has been carried out with a water-like wetting phase ($\mu_w = 1$ mPa · s, $K_w = 2.15$ GPa) and an oil-like non-wetting phase ($\mu_n = 0.45$ mPa · s, $K_n = 1.5$ GPa). The porous solid has the following properties: Porosity $n_f = 0.2$, Poisson ratio $\nu = 0.2$, bulk modulus $K_s = 36$ GPa, Biot coefficient $\alpha = 1.0$,

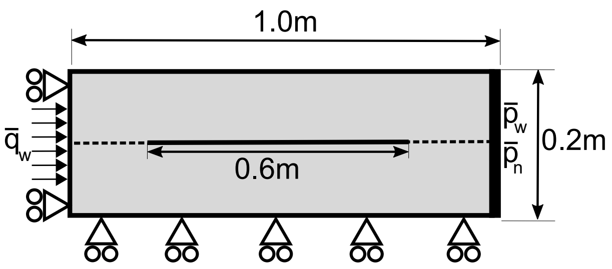

Figure 3: Overview of the single fracture case.

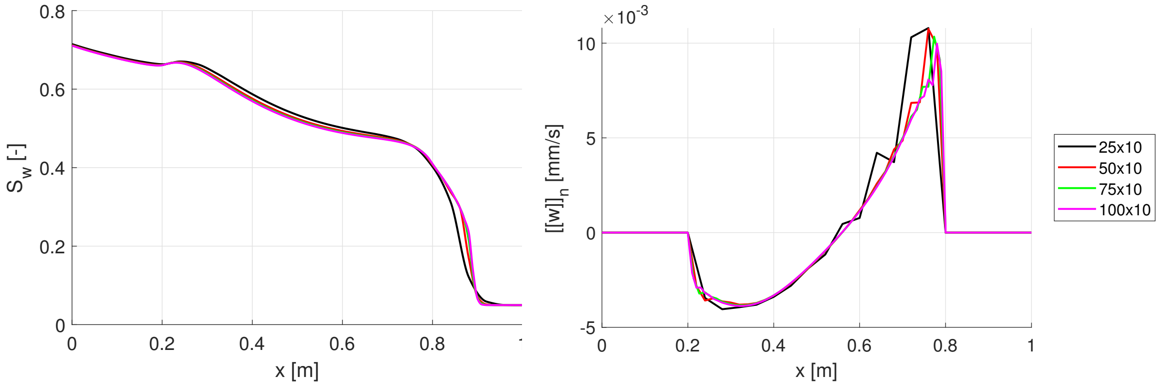

(a) Wetting phase saturation

(b) Non-wetting phase fracture outflow

Figure 4: Selected results along the discontinuity from the mesh refinement study, using the bubbly flow model. Results given for $E = 20$GPa, $t = 2.5$hours

and intrinsic permeability $k = 10^{-12}$ m^2. The Young's modulus $E = 20$ GPa in Section 4.1, and has been varied between 1 GPa and 1000 GPa in Section 4.2. The constant used for the saturation relations, Eq. 2, is $B = 10^5$ Pa.

The initial interstitial pressures were $p_w = 0$ MPa and $p_n = 0.3$ MPa, resulting in an initial degree of saturation of $S_w = 0.05$. A wetting phase inflow, $\bar{q}_w = 10^{-5}$ m/s, is imposed on the left edge. This inflow will displace the non-wetting phase towards the right edge, on which a constant pressure boundary condition (equal to the initial pressure) is imposed to allow for an outflow of the non-wetting and wetting phases. The simulations have been carried out using a time-step size $\Delta t = 25$ s and dummy stiffnesses $k_n = k_s = 5 \cdot 10^3$ GPa for the non-fractured interface elements. The fracture has been assumed stationary without cohesive tractions.

The domain has been discretised using 100×10 elements , using quartic NURBS for the solid displacements, and cubic NURBS for the wetting and non-wetting pressures. To determine this required number of elements, a similar analysis as in [45] was performed. ~~The rather large number of horizontal elements has been chosen to obtain an accurate fracture inflow from the sub-grid model~~ Selected results from this mesh refinement study are shown in Figure 4. Due to the higher order inter-element continuity of NURBS, the fracture outflow remains continuous. While a coarse mesh suffices to describe the saturation and pressures, a finer mesh was needed to accurately describe the fracture outflow.

4.1. Comparison of the fracture flow models

The degree of saturation for the wetting phase is shown in Figure 5 for the separated flow fracture model. The fracture transports a large amount of fluid, whereas the fluid is transported much more slowly inside the surrounding porous medium. This causes the wetting phase to diffuse both horizontally and vertically from the fracture , as shown in Figure 6, resulting in a decreased saturation gradient normal to the fracture.

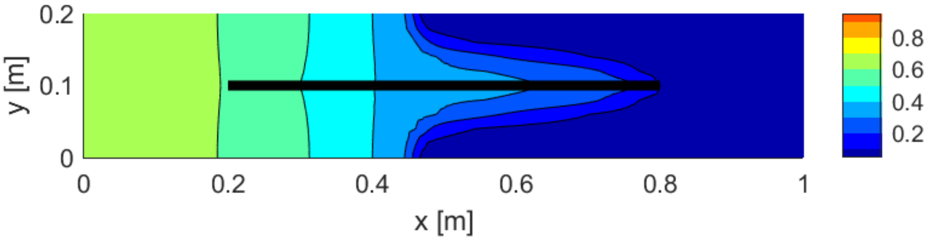

(a) $t = 1.5$ hours

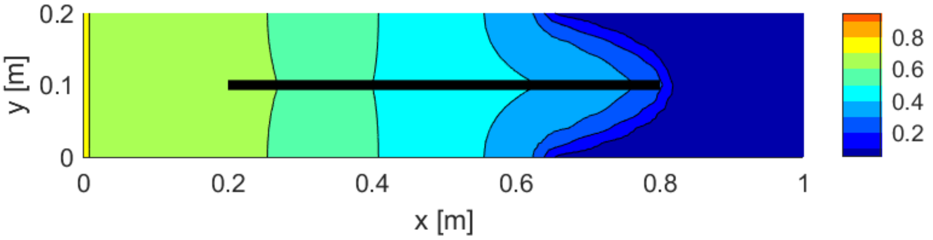

(b) $t = 2$ hours

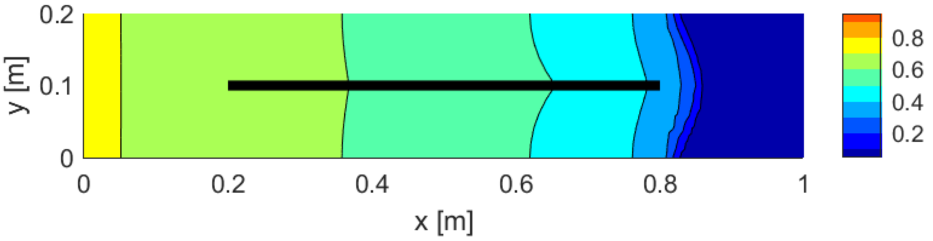

(c) $t = 2.5$ hours

Figure 5: Degree of saturation for the wetting phase inside the porous medium using the separated flow model.

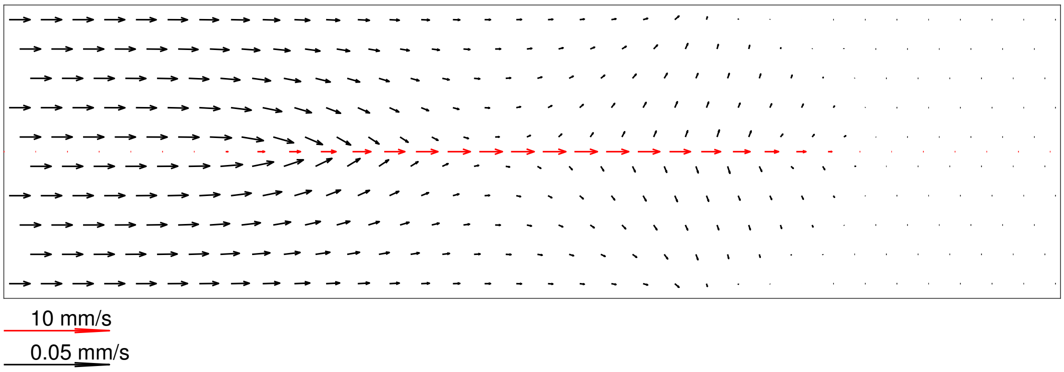

(a) Wetting phase

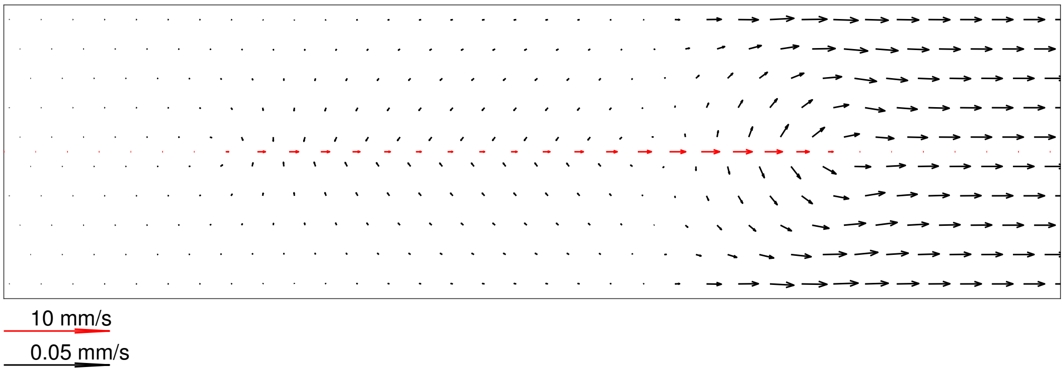

(b) Non-Wetting phase

Figure 6: Fluid flux inside the porous medium (black) and maximum fluid velocity inside the fracture (red) at $t = 2$ hours using the separated flow model.

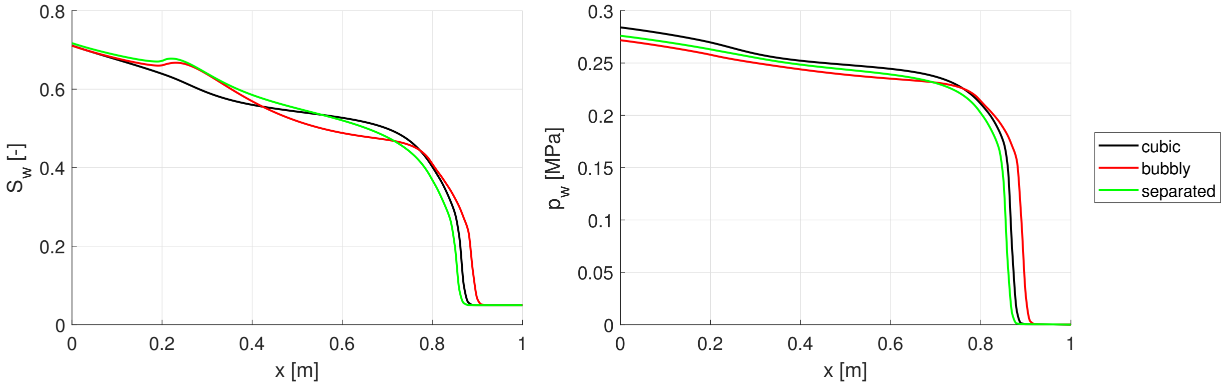

(a) Wetting phase saturation

(b) Wetting phase pressure

Figure 7: Degree of saturation and pressure along the discontinuity at $t = 2.5$ hours.

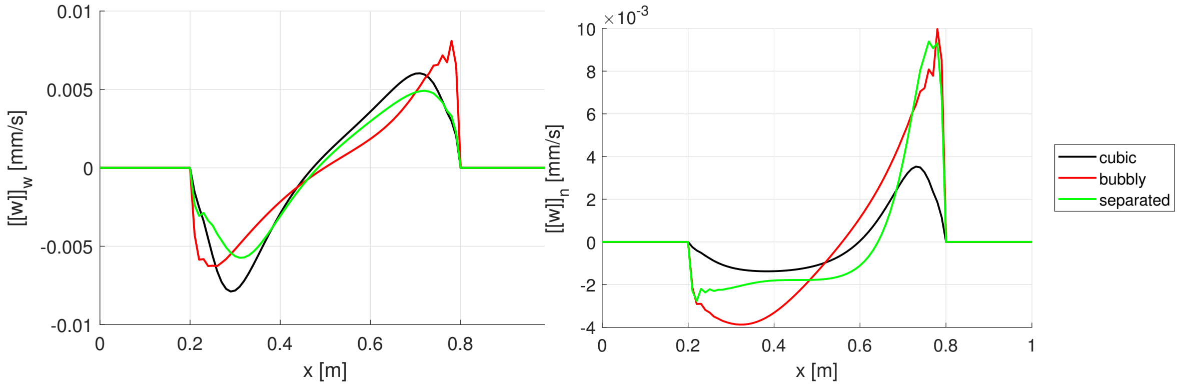

(a) Wetting phase

(b) Non-wetting phase

Figure 8: Fracture outflow velocity for the wetting and non-wetting phases at $t = 2.5$ hours.

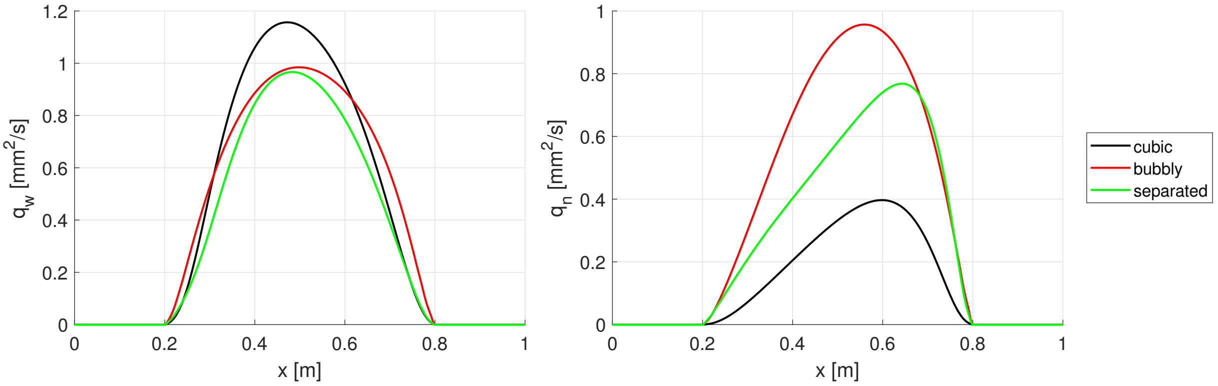

(a) Wetting phase

(b) Non-wetting phase

Figure 9: Fluid transported inside the fracture for the wetting and non-wetting phases at $t = 2.5$ hours, obtained from post-processing.

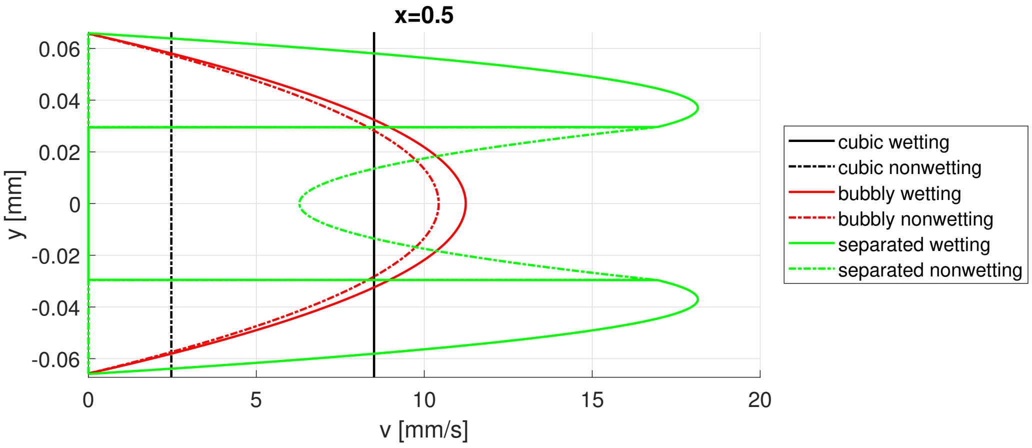

Figure 10: Velocity profile of the phases inside the fracture at $x = 0.5m$, $t = 2.5$ hours, obtained from post-processing.

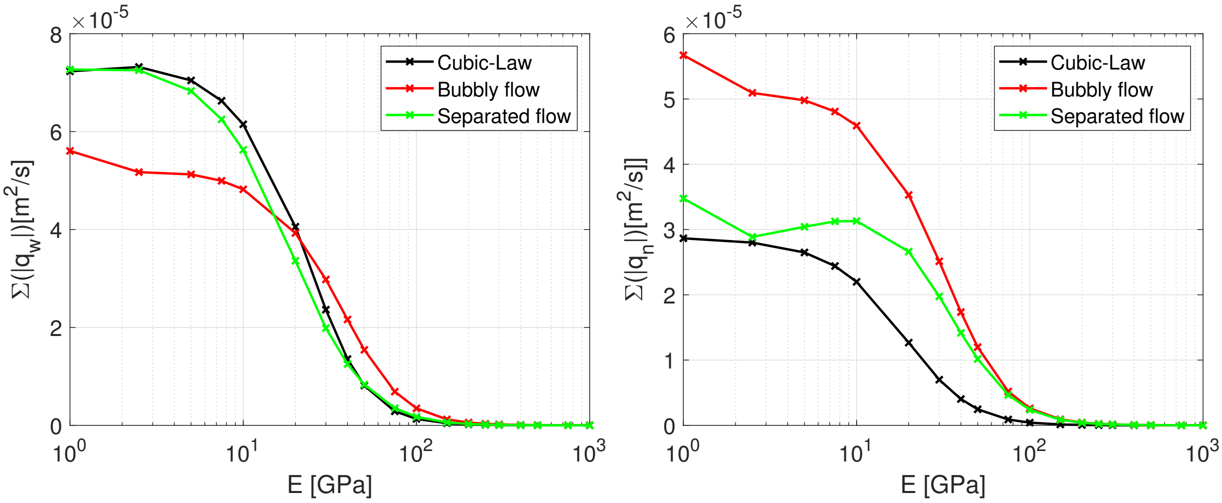

(a) Wetting phase

(b) Non-wetting phase

Figure 11: Total amount of fluid transported inside the fracture ~~for~~ as a function of the Young's modulus at $t = 2.5$ hours.

This behaviour was observed for all the fracture flow models. Furthermore, the fracture opening height was equal for all models, with a maximum opening height at $t = 2.5$ hours of $h = 0.13$ mm.

The degree of saturation for the wetting phase is given in Figure 7a along the discontinuity for the different fracture flow models. The separated flow model shows a higher saturation near the left fracture tip compared to the cubic law model, while the location of the front of the wetting phase is similar. This is in contrast to the bubbly flow model. While showing a similar increase in saturation near the left fracture tip, a lower degree of saturation occurs in the middle of the fracture and the saturation front has advanced further. A similar behaviour is seen for the interstitial pressure of the wetting phase, Figure 7b.

The fracture outflow at $t = 2.5$ hours is shown in Figure 8. While the outflow of the wetting phase shows small differences between the models, large differences are seen for the non-wetting phase outflow. These differences are caused by the interaction between the phases, with both the bubbly flow model and the separated flow model dragging along the non-wetting phase, which has a low pressure gradient along the fracture. This causes a slight decrease in fracture outflow for the wetting phases, since this phase is held back by the non-wetting phase, while increasing the amount of non-wetting phase transported. This is confirmed by the fluid flux inside the fracture as seen in Figure 9. This fluid flux is obtained by post-processing, since the interior of the fracture is not simulated explicitly.

The velocity profiles inside the fracture, Figure 10, are also obtained by post-processing. The cubic flow model shows a constant velocity, since the cubic law and the empirical correction factor for multiphase flows only describe the total fluid flux. The velocity profiles for the separated flow show the non-wetting phase being dragged against its pressure gradient by the wetting phase, slowing down the velocity of the wetting phase while increasing the non-wetting phase velocity. The bubbly flow model has a similar behaviour due to the volume-averaging of the pressure gradient. However, different from the separated flow model, the fluid flux of the non-wetting phase is higher than the wetting phase due to the distribution of the total velocity being solely based on the degree of saturation of the phases.

4.2. The effect of the sub-grid model

The effect of the fracture on the surrounding porous medium has been investigated by varying the Young's modulus, causing a change in fracture height, which scales approximately linearly with the Young's modulus. This causes a change in fluid transported inside the fracture and allows the effect of the fracture to be varied from dominating the fluid transport to having a negligible influence on the fluid transport inside the porous medium.

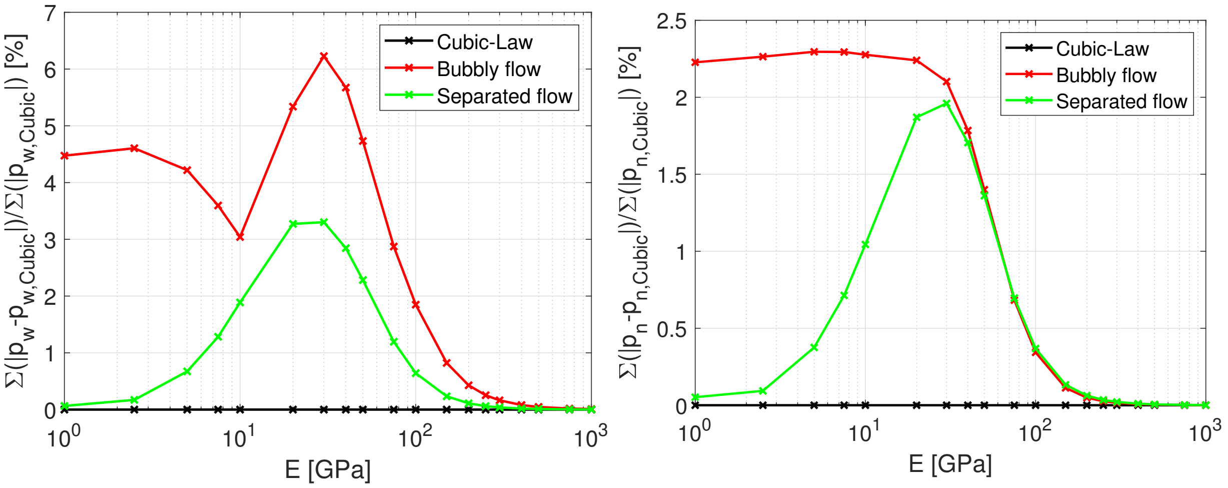

(a) Wetting phase

(b) Non-wetting phase

Figure 12: Relative differences in the pressure along the discontinuity when varying Young's modulus at $t = 2.5$ hours.

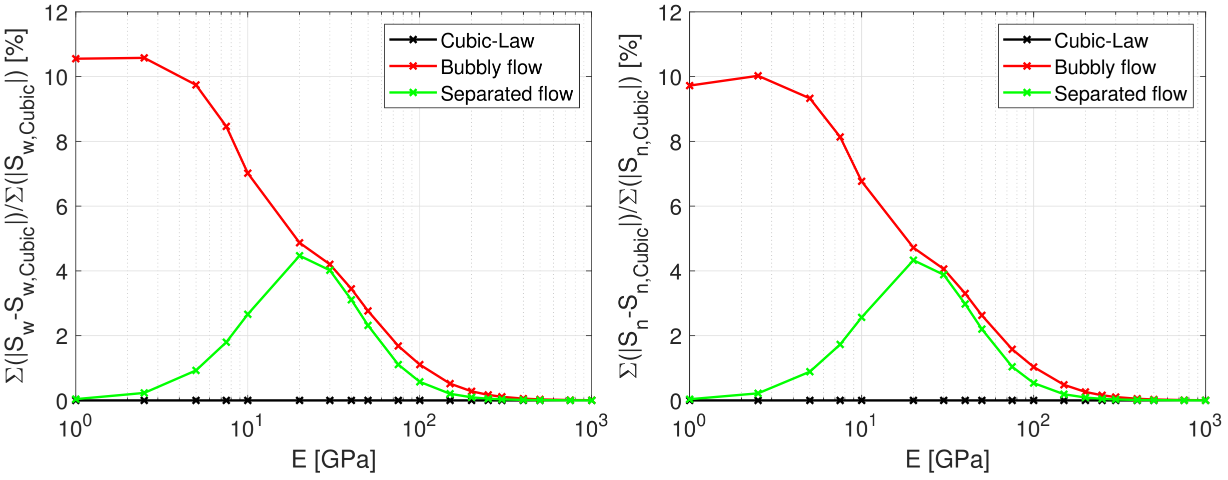

(a) Wetting phase

(b) Non-wetting phase

Figure 13: Relative differences for the degree of saturation along the discontinuity when varying Young's modulus at $t = 2.5$ hours.

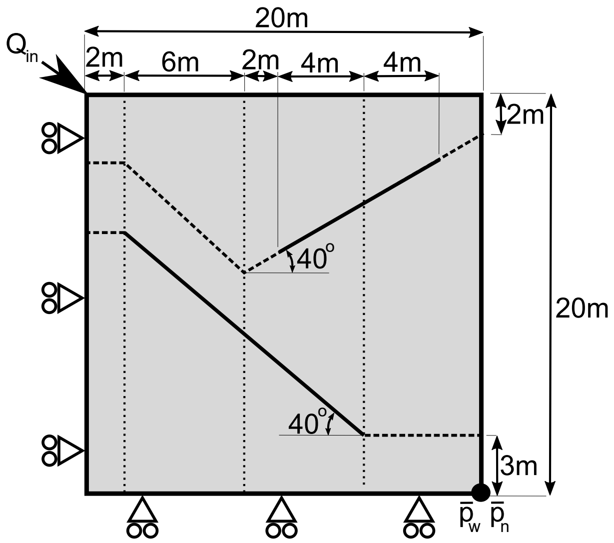

Figure 14: Overview of the multiple fracture case. Dashed lines indicate the C^{-1} discontinuities, while the dotted lines indicate C^{0} continuity lines.

The resulting fluid transport inside the fracture is shown in Figure 11. For high values of the Young's modulus, the flux is small, and therefore neither the fracture, nor the choice of the flow model influence the results. However for low values of the Young's modulus large amounts of fluid are transported inside the fracture. Comparing the separated flow model with the cubic law model shows marginal differences in the flux of the wetting phase fluid, while any difference disappears in limiting cases where the fracture flow or the flow in the porous medium dominate. The bubbly flow model, however, shows large differences, for the fluxes of the wetting as well as for the non-wetting phases.

Figure 12 shows the difference in pressures of the interstitial fluids along the discontinuity, and Figure 13 shows the degree of saturation. Due to the negligible differences in fluid flux between the separated and cubic law models at low and high Young's moduli, no difference in pressure and saturation occurs at these limits. In the intermediate range of Young's moduli, small differences in pressure and saturation occur, with a maximum around $E = 20$ GPa, which correspond to the small differences in Figure 7-9.

The difference in fluid flux between the bubbly flow model and cubic law model does not disappear for low values of the Young's modulus, and therefore neither does the difference between the degrees of saturation and the pressures in the fracture flow dominated regime. For high values of the Young's modulus this difference does disappear, however, and the volume-averaged bubbly flow model shows a similar behaviour of the pressure difference and the difference in the degree of saturation as observed for the separated flow model. This indicates that the coupling between the wetting and non-wetting fluid fluxes due to the volume averaging used in this model is sufficiently enough to move extra non-wetting fluid towards and through the fracture. This results in a local decrease in non-wetting phase pressure around the fracture tip (not shown here), and therefore a large increase in the degree of saturation of the wetting phase. Since this effect depends on the fluid transported inside the fracture, the decrease in pressure becomes more pronounced for higher values of the fracture opening height, and therefore does not disappear in the fracture dominated flow limit. Thus, the inclusion of the interaction between the wetting and the non-wetting phase can significantly alter the degree of saturation.

5. Some further applications

To illustrate the effect of including interaction between the wetting and non-wetting phases, and to show the influence of the choice of fracture flow model, two cases more representative of real-world applications

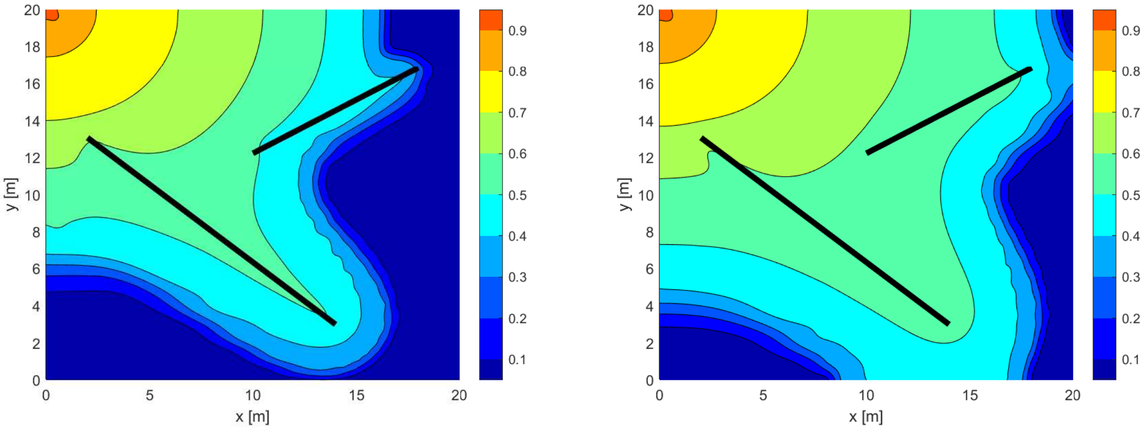

(a) $t = 30$ days (b) $t = 40$ days

Figure 15: Degree of saturation for the wetting phase using the cubic-law model.

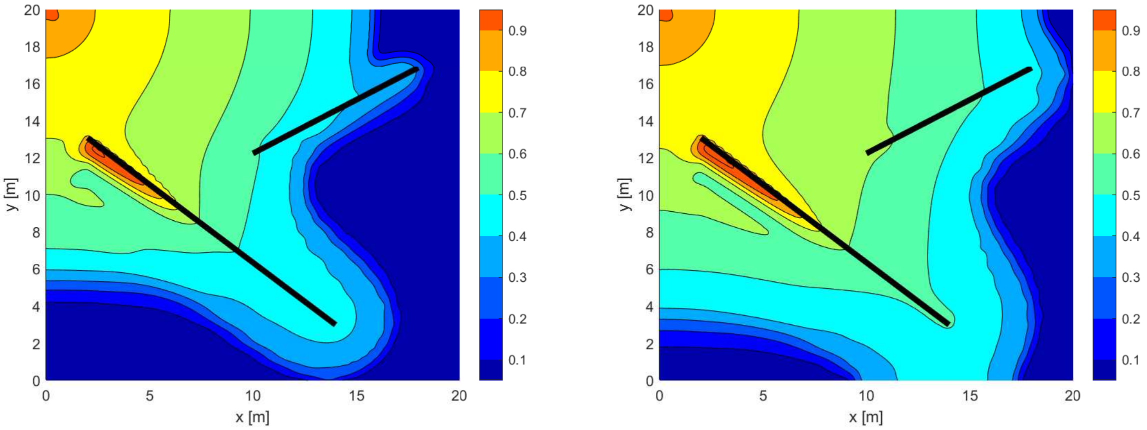

(a) $t = 30$ days (b) $t = 40$ days

Figure 16: Degree of saturation for the wetting phase using the volume-averaged bubbly flow model.

were simulated: Underground oil recovery and gas/CO_2 storage. These cases were simulated using a geometry containing two diagonal fractures, as shown in Figure 14. Since NURBS were used for the meshing, C^0 continuity lines were inserted to allow for sharp changes in mesh-line direction. Similar to the previous case, the fractures were assumed stationary and no cohesive tractions were considered. The domain was discretised using 50×30 elements, and a time-step of $\Delta t = 1000$ s was used for both cases.

5.1. Oil-water

We now consider the case of water and oil inside porous rocks, using the same properties as in Section 4. A wetting phase inflow of $Q_{in} = 10^{-5}$ m^3/s is imposed in the top-left corner, while a constant pressure of $p_w = 0.0$ MPa, $p_n = 0.3$ MPa ($S_w = 0.05$) is imposed on the bottom right corner to simulate water being injected for displacing the oil towards a free-flowing outlet. The initial degree of saturation is set equal to the outflow boundary condition, $S_w = 0.05$.

The degree of saturation of the wetting phase is shown in figure 15 after 30 and 40 days using the cubic law flow model. While the bottom fracture enhances the water transport, it also results in a pocket of oil in the bottom right being isolated from the outlet. The top right fracture blocks part of the fluid flow,

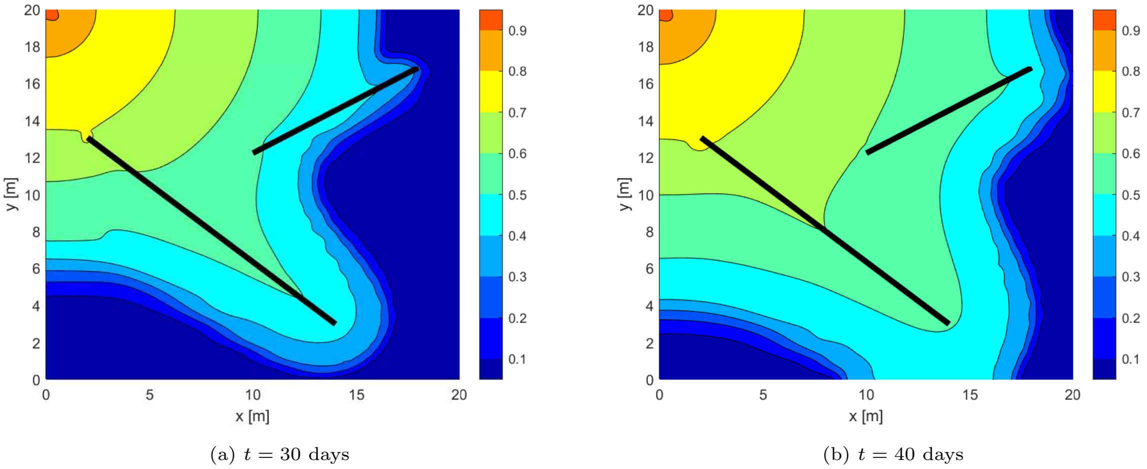

(a) $t = 30$ days

(b) $t = 40$ days

Figure 17: Degree of saturation for the wetting phase using the separated flow model.

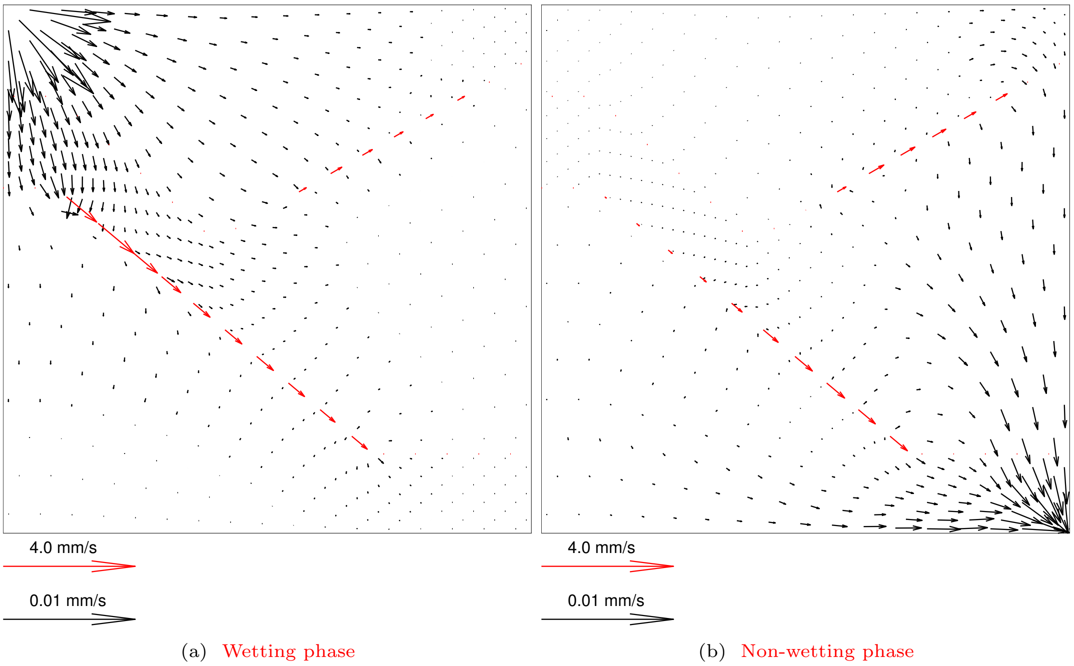

(a) Wetting phase

(b) Non-wetting phase

Figure 18: Fluid flux inside the porous medium (black) and maximum velocity inside the fracture (red) using the bubbly fracture flow model at $t = 30$ days.

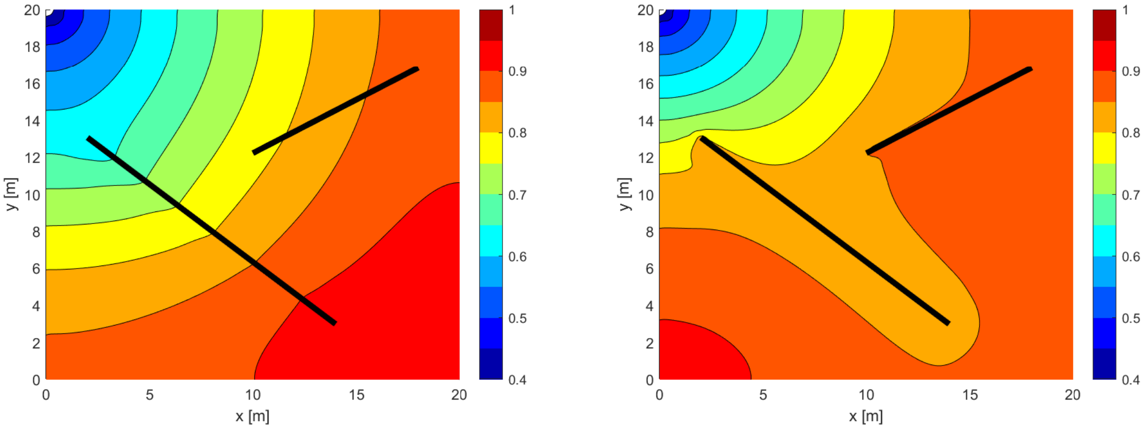

(a) Volume-averaged bubbly flow model

(b) Cubic law and separated flow models

Figure 19: Degree of saturation for the wetting phase for air/water at $t = 15.5$ hours.

equalising the degree of saturation along the fracture and thereby preventing the oil at the top left from becoming separated from the outlet.

Figure 16 shows the resulting degree of saturation using the volume-averaged bubbly flow model. As was the case with the simplified example, the water inside the fracture drags the oil along, creating a local minimum in the non-wetting pressure and thereby causing a local increase in the saturation near the fracture. This saturation is higher on the bottom of the fracture compared to the top due to the water displacing the oil towards the fracture near the top. This occurs less at the bottom of the fracture. Comparing these results to the simulation using the cubic law shows that this local increase in the degree of saturation is accompanied with a coupling between the water and oil flows inside the fracture.

The separated flow model, Figure 17, shows a balance between the coupling observed using the bubbly flow model, and fluids purely flowing in the same direction as their pressure gradients observed for the cubic law. The coupling still causes a small increase in the degree of saturation along the fracture compared to the cubic law, but this increase is modest compared to the bubbly flow. Likewise, the water flow is not slowed down as much due to the interaction with the oil, resulting in a slightly higher degree of saturation near the end of the fracture.

5.2. Air-water

The second application is underground gas storage. In this case, air ($\mu_n = 2 \cdot 10^{-5}$ Pa$\cdot$s, $K_n = 0.1$ MPa) is injected in the top left corner with an inflow of $Q_{in} = 5 \cdot 10^{-2}$ m^3/s. The domain has an initial degree of saturation for the water $S_w = 0.9$ ($p_w = -0.9$ MPa, $p_n = 8.1$ MPa), and the pressure and the degree of saturation at the outlet in the bottom right corner are imposed to be constant. The porous material is assumed to be sandstone-like, using $k = 10^{-13}$ m^2 and all other material properties equal to the solid properties used in Section 4. In order to better represent the gas-water interactions inside the porous medium, the saturation relation of Eq. (2) is replaced with the Van Genuchten relation [49, 67]:

$$S_w = \left(1 - \left(\frac{p_c}{p_{ref}}\right)^{\frac{1}{1-m}}\right)^{-m} \tag{69}$$

and instead of Eq. (12) the relative permeability relations for the flow inside the porous medium read:

$$k_{rw} = S_w^{1/2}\left(1 - \left(1 - S_w^{\frac{1}{m}}\right)^m\right)^2 \tag{70}$$

$$k_{rn} = (1 - S_w)^{1/2}\left(1 - S_w^{\frac{1}{m}}\right)^{2m} \tag{71}$$

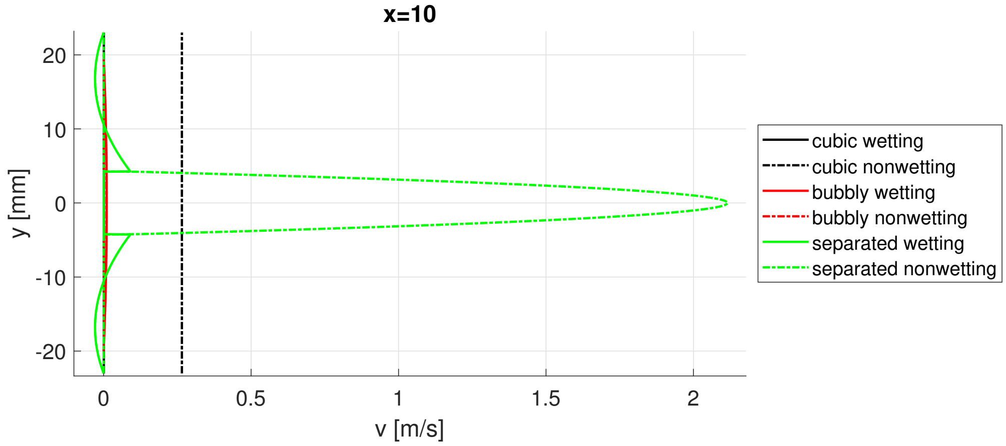

Figure 20: Velocity profile of the phases inside the bottom fracture at $x = 10.0m$, t = 15.5 hours, obtained from post-processing.

using $m = 0.4369$ and $p_{ref} = 18.6\text{MPa}$.

The degree of saturation which has been computed using the separated and cubic-law flow models is shown in Figure 19b. Due to the low viscosity of the gas, the fractures transport large amounts of gas and thereby equalise the degree of saturation along the discontinuity. This occurs for both the cubic-law and the separated flow model. However, use of the volume-averaged bubbly flow model results only a small influence of the fracture on the saturation within the porous media, see Figure 19a. This contrast with the other models is caused by the fact that the volume averaging markedly increases the effective viscosity of the gas phase due to the high degree of water saturation, which limits the air flow through the fracture.

The fluid velocity profiles resulting from post-processing are shown in Figure 20. The velocity profile for the cubic law shows a high air velocity, while the water velocity is low. The velocity profiles for the separated flow model show a similarly high air velocity, with about an equal amount of air being transported. While near to no water is transported using the separated flow model, the air dragging the water along causes a negative pressure gradient, resulting in a back-flow of water near the fracture walls while the water flows in the same direction as the air near the water-air interface.

6. Concluding remarks

Sub-grid models capable of representing two-phase flow within a fracture have been presented. These models are able to include multiphase flow within fractures, without the need to explicitly simulate the interior of these fractures. This allows for the discretisation of large domains, while still including the fluid transported by fractures with a small opening height. It is shown that these models are capable of including the interaction between the wetting and non-wetting phases inside the fracture, and allow for post-processing to obtain velocity profiles and fluid fluxes.

These sub-grid models have been compared to the cubic-law, which is commonly used to represent the fracture flow. It was shown that assuming a volume-averaged bubbly flow or a separated flow inside the fracture allows the high pressure gradient phase to drag along the low pressure gradient phase, thus increasing the velocity of the low gradient phase and slowing down the high gradient phase. While this effect was stronger for the bubbly flow model, it resulted in a local minimum in the non-wetting phase pressure. The separated flow model provides results which are more similar to the cubic-law, but still show the non-wetting phase being dragged along with the wetting phase. Simulations for different values of Young's modulus have shown the solution to be independent of the sub-grid model when the fracture has a negligible effect, with the bubbly flow model providing results which are different from those of the separated and cubic-law models for fracture-dominated problems.

Two cases which are more representative of real-world applications, namely oil recovery and underground gas storage, have been simulated to show the effect on the degrees of saturation. It has been shown that the volume-averaged bubbly flow model resultes in a local increase in the degree of saturation by the wetting phase, dragging along the non-wetting phase. Furthermore, the volume averaging results in low air velocities for the case of underground gas storage. In contrast, the separated flow model shows results comparable to the cubic law. Velocity profiles inside the fractures show a local back-flow inside the fracture while retaining an overall positive fluid flux. This highlights the ability of the sub-grid fracture models to obtain a detailed description of the fluid behaviour inside the discontinuity by post-processing, while obviating the need to discretise the interior of the fracture.

Acknowledgement Financial support through H2020 European Research Council Advanced Grant 664734 ”PoroFrac” is gratefully acknowledged.

Appendix A. Tangential stiffness sub-matrices

The system of non-linear equations is solved using a Newton-Raphson iterative method. For this, the discretised equations are linearised as:

$$\begin{bmatrix} \boldsymbol{K} + \boldsymbol{K}_d & \boldsymbol{Q}_{sw} + \boldsymbol{Q}_{d,sw} & \boldsymbol{Q}_{sn} + \boldsymbol{Q}_{d,sn} \\ \boldsymbol{Q}_{ws} + \boldsymbol{Q}_{d,ws} + \boldsymbol{H}_{d,ws} & \boldsymbol{H}_{ww} + \boldsymbol{C}_{ww} + \boldsymbol{Q}_{ww} + \boldsymbol{Q}_{d,ww} + \boldsymbol{H}_{d,ww} & \boldsymbol{H}_{wn} + \boldsymbol{C}_{wn} + \boldsymbol{Q}_{wn} + \boldsymbol{Q}_{d,wn} + \boldsymbol{H}_{d,wn} \\ \boldsymbol{Q}_{ns} + \boldsymbol{Q}_{d,ns} + \boldsymbol{H}_{d,ns} & \boldsymbol{H}_{nw} + \boldsymbol{C}_{nw} + \boldsymbol{Q}_{nw} + \boldsymbol{Q}_{d,nw} + \boldsymbol{H}_{d,nw} & \boldsymbol{H}_{nn} + \boldsymbol{C}_{nn} + \boldsymbol{Q}_{nn} + \boldsymbol{Q}_{d,nn} + \boldsymbol{H}_{d,nn} \end{bmatrix} \begin{bmatrix} \mathrm{d}\boldsymbol{u} \\ \mathrm{d}\boldsymbol{p}_w \\ \mathrm{d}\boldsymbol{p}_n \end{bmatrix}$$

$$= \begin{bmatrix} \boldsymbol{f}_{ext} \\ \boldsymbol{q}_{w,ext} \\ \boldsymbol{q}_{n,ext} \end{bmatrix} - \begin{bmatrix} \boldsymbol{f}_{int} + \boldsymbol{f}_d \\ \boldsymbol{q}_{w,int} + \boldsymbol{q}_{w,d} \\ \boldsymbol{q}_{n,int} + \boldsymbol{q}_{n,d} \end{bmatrix} \tag{A.1}$$

with the external and internal forces defined in Eq. 48, 49, and 51, and the fluxes defined in Eq. 54-57.

The tangential stiffness sub-matrices related to the interior forces and fluxes are given by:

$$\boldsymbol{K} = \int_{\Omega} \boldsymbol{B}^T \boldsymbol{D} \boldsymbol{B} \mathrm{d}\Omega \tag{A.2}$$

$$\boldsymbol{Q}_{sw} = - \int_{\Omega} \alpha \left(S_w - p_w \frac{\partial S_w}{\partial p_c} \right) \boldsymbol{B}^T \boldsymbol{m} \boldsymbol{N}_w + \alpha \left(p_n \frac{\partial S_w}{\partial p_c} \right) \boldsymbol{B}^T \boldsymbol{m} \boldsymbol{N}_n \mathrm{d}\Omega \tag{A.3}$$

$$\boldsymbol{Q}_{sn} = - \int_{\Omega} \alpha \left(S_n - p_n \frac{\partial S_w}{\partial p_c} \right) \boldsymbol{B}^T \boldsymbol{m} \boldsymbol{N}_n + \alpha \left(p_w \frac{\partial S_w}{\partial p_c} \right) \boldsymbol{B}^T \boldsymbol{m} \boldsymbol{N}_w \mathrm{d}\Omega \tag{A.4}$$

$$\boldsymbol{Q}_{ws} = - \int_{\Omega} \alpha S_w \boldsymbol{N}_w^T \boldsymbol{m}^T \boldsymbol{B} \mathrm{d}\Omega \tag{A.5}$$

$$\boldsymbol{Q}_{ww} = \int_{\Omega} \alpha \left(\boldsymbol{m}^T \boldsymbol{B} \left(\boldsymbol{u}^{t+\Delta t} - \boldsymbol{u}^t \right) \right) \frac{\partial S_w}{\partial p_c} \boldsymbol{N}_w^T \boldsymbol{N}_w \mathrm{d}\Omega \tag{A.6}$$

$$\boldsymbol{Q}_{wn} = - \int_{\Omega} \alpha \left(\boldsymbol{m}^T \boldsymbol{B} \left(\boldsymbol{u}^{t+\Delta t} - \boldsymbol{u}^t \right) \right) \frac{\partial S_w}{\partial p_c} \boldsymbol{N}_w^T \boldsymbol{N}_n \mathrm{d}\Omega \tag{A.7}$$

$$\boldsymbol{Q}_{ns} = - \int_{\Omega} \alpha S_n \boldsymbol{N}_n^T \boldsymbol{m}^T \boldsymbol{B} \mathrm{d}\Omega \tag{A.8}$$

$$\boldsymbol{Q}_{nw} = - \int_{\Omega} \alpha \left(\boldsymbol{m}^T \boldsymbol{B} \left(\boldsymbol{u}^{t+\Delta t} - \boldsymbol{u}^t \right) \right) \frac{\partial S_w}{\partial p_c} \boldsymbol{N}_n^T \boldsymbol{N}_w \mathrm{d}\Omega \tag{A.9}$$

$$\boldsymbol{Q}_{nn} = \int_{\Omega} \alpha \left(\boldsymbol{m}^T \boldsymbol{B} \left(\boldsymbol{u}^{t+\Delta t} - \boldsymbol{u}^t \right) \right) \frac{\partial S_w}{\partial p_c} \boldsymbol{N}_n^T \boldsymbol{N}_n \mathrm{d}\Omega \tag{A.10}$$

$$\boldsymbol{C}_{ww} = - \int_{\Omega} \left(\frac{1}{M_{ww}} - \left(p_w^{t+\Delta t} - p_w^t \right) \frac{\partial 1/M_{ww}}{\partial p_c} - \left(p_n^{t+\Delta t} - p_n^t \right) \frac{\partial 1/M_{wn}}{\partial p_c} \right) \boldsymbol{N}_w^T \boldsymbol{N}_w \mathrm{d}\Omega \tag{A.11}$$

$$\boldsymbol{C}_{wn} = - \int_{\Omega} \left(\frac{1}{M_{wn}} + \left(p_w^{t+\Delta t} - p_w^t \right) \frac{\partial 1/M_{ww}}{\partial p_c} + \left(p_n^{t+\Delta t} - p_n^t \right) \frac{\partial 1/M_{wn}}{\partial p_c} \right) \boldsymbol{N}_w^T \boldsymbol{N}_n \mathrm{d}\Omega \tag{A.12}$$

$$\boldsymbol{C}_{nw} = - \int_{\Omega} \left(\frac{1}{M_{nw}} - \left(p_w^{t+\Delta t} - p_w^t \right) \frac{\partial 1/M_{nw}}{\partial p_c} - \left(p_n^{t+\Delta t} - p_n^t \right) \frac{\partial 1/M_{nn}}{\partial p_c} \right) \boldsymbol{N}_n^T \boldsymbol{N}_w \mathrm{d}\Omega \tag{A.13}$$

$$\boldsymbol{C}_{nn} = - \int_{\Omega} \left(\frac{1}{M_{nn}} + \left(p_w^{t+\Delta t} - p_w^t \right) \frac{\partial 1/M_{nw}}{\partial p_c} + \left(p_n^{t+\Delta t} - p_n^t \right) \frac{\partial 1/M_{nn}}{\partial p_c} \right) \boldsymbol{N}_n^T \boldsymbol{N}_w \mathrm{d}\Omega \tag{A.14}$$

$$\boldsymbol{H}_{ww} = -\Delta t \int_{\Omega} k_w k_{rw} \left(\boldsymbol{\nabla} \boldsymbol{N}_w \right)^T \boldsymbol{\nabla} \boldsymbol{N}_w - k_w \frac{\partial k_{rw}}{\partial S_w} \frac{\partial S_w}{\partial p_c} \left(\left(\boldsymbol{\nabla} \boldsymbol{N}_w \boldsymbol{p}_w \right)^T \boldsymbol{\nabla} \boldsymbol{N}_w \right)^T \boldsymbol{N}_w \mathrm{d}\Omega \tag{A.15}$$

$$\boldsymbol{H}_{wn} = -\Delta t \int_{\Omega} k_w \frac{\partial k_{rw}}{\partial S_w} \frac{\partial S_w}{\partial p_c} \left(\left(\boldsymbol{\nabla} \boldsymbol{N}_w \boldsymbol{p}_w \right)^T \boldsymbol{\nabla} \boldsymbol{N}_w \right)^T \boldsymbol{N}_n \mathrm{d}\Omega \tag{A.16}$$

$$\boldsymbol{H}_{nw} = -\Delta t \int_{\Omega} k_n \frac{\partial k_{rn}}{\partial S_w} \frac{\partial S_w}{\partial p_c} \left(\left(\boldsymbol{\nabla} \boldsymbol{N}_n \boldsymbol{p}_n \right)^T \boldsymbol{\nabla} \boldsymbol{N}_n \right)^T \boldsymbol{N}_w \mathrm{d}\Omega \tag{A.17}$$

$$\boldsymbol{H}_{nn} = -\Delta t \int_{\Omega} k_n k_{rn} \left(\boldsymbol{\nabla} \boldsymbol{N}_n \right)^T \boldsymbol{\nabla} \boldsymbol{N}_n + k_n \frac{\partial k_{rn}}{\partial S_w} \frac{\partial S_w}{\partial p_c} \left(\left(\boldsymbol{\nabla} \boldsymbol{N}_n \boldsymbol{p}_n \right)^T \boldsymbol{\nabla} \boldsymbol{N}_n \right)^T \boldsymbol{N}_n \mathrm{d}\Omega \tag{A.18}$$

with all variables determined by using the updated displacements and pressures, and all values determined in the integration points.

The tangential stiffness sub-matrices related to the forces at the discontinuity are given by:

$$\boldsymbol{K}_d = \int_{\Gamma_d} \boldsymbol{N}_d^T \boldsymbol{R} \boldsymbol{D}_d \boldsymbol{R} \boldsymbol{N}_d \mathrm{d}\Gamma \tag{A.19}$$

$$\boldsymbol{Q}_{d,sw} = - \int_{\Gamma_d} \left(S_w + (p_n - p_w) \frac{\partial S_w}{\partial p_c} \right) \boldsymbol{N}_d^T \boldsymbol{n}_{\Gamma_d} \boldsymbol{N}_w \mathrm{d}\Gamma \tag{A.20}$$

$$\boldsymbol{Q}_{d,sn} = - \int_{\Gamma_d} \left(S_n - (p_n - p_w) \frac{\partial S_w}{\partial p_c} \right) \boldsymbol{N}_d^T \boldsymbol{n}_{\Gamma_d} \boldsymbol{N}_n \mathrm{d}\Gamma \tag{A.21}$$

The terms related to the fluid absorbed by the fracture opening are independent of the fracture flow model, and given by:

$$\boldsymbol{Q}_{d,ws} = -\int_{\Gamma_d} \left(S_w + (S_w^{t+\Delta t} - S_w^t\right) \boldsymbol{N}_w^T \boldsymbol{n}_{\Gamma_d}^T \boldsymbol{N}_d \mathrm{d}\Gamma \tag{A.22}$$

$$\boldsymbol{Q}_{d,ww} = \int_{\Gamma_d} \left(\frac{\partial S_w}{\partial p_c} \left(\boldsymbol{n}_{\Gamma_d}^T \boldsymbol{N}_d \left(\boldsymbol{u}^{t+\Delta t} - \boldsymbol{u}^t\right)\right) + \left(\boldsymbol{n}_{\Gamma_d}^T \boldsymbol{N}_d \boldsymbol{u}\right) \frac{\partial S_w}{\partial p_c}\right) \boldsymbol{N}_w^T \boldsymbol{N}_w \mathrm{d}\Gamma \tag{A.23}$$

$$\boldsymbol{Q}_{d,wn} = -\int_{\Gamma_d} \left(\frac{\partial S_w}{\partial p_c} \left(\boldsymbol{n}_{\Gamma_d}^T \boldsymbol{N}_d \left(\boldsymbol{u}^{t+\Delta t} - \boldsymbol{u}^t\right)\right) + \left(\boldsymbol{n}_{\Gamma_d}^T \boldsymbol{N}_d \boldsymbol{u}\right) \frac{\partial S_w}{\partial p_c}\right) \boldsymbol{N}_w^T \boldsymbol{N}_n \mathrm{d}\Gamma \tag{A.24}$$

$$\boldsymbol{Q}_{d,ns} = -\int_{\Gamma_d} \left(S_n + (S_n^{t+\Delta t} - S_n^t\right) \boldsymbol{N}_n^T \boldsymbol{n}_{\Gamma_d}^T \boldsymbol{N}_d \mathrm{d}\Gamma \tag{A.25}$$

$$\boldsymbol{Q}_{d,nw} = -\int_{\Gamma_d} \left(\frac{\partial S_w}{\partial p_c} \left(\boldsymbol{n}_{\Gamma_d}^T \boldsymbol{N}_d \left(\boldsymbol{u}^{t+\Delta t} - \boldsymbol{u}^t\right)\right) + \left(\boldsymbol{n}_{\Gamma_d}^T \boldsymbol{N}_d \boldsymbol{u}\right) \frac{\partial S_w}{\partial p_c}\right) \boldsymbol{N}_n^T \boldsymbol{N}_w \mathrm{d}\Gamma \tag{A.26}$$

$$\boldsymbol{Q}_{d,nn} = \int_{\Gamma_d} \left(\frac{\partial S_w}{\partial p_c} \left(\boldsymbol{n}_{\Gamma_d}^T \boldsymbol{N}_d \left(\boldsymbol{u}^{t+\Delta t} - \boldsymbol{u}^t\right)\right) + \left(\boldsymbol{n}_{\Gamma_d}^T \boldsymbol{N}_d \boldsymbol{u}\right) \frac{\partial S_w}{\partial p_c}\right) \boldsymbol{N}_n^T \boldsymbol{N}_n \mathrm{d}\Gamma \tag{A.27}$$

The final terms, related to the sub-grid model used to model the fracture in and outflow, depend on the flow type assumed for the flow inside the fracture. For the cubic-law model, the tangential stiffness matrices are given by:

$$\boldsymbol{H}_{d,ws}^{cubic} = -\Delta t \int_{\Gamma_d} \frac{S_w^3}{4\mu_w} \left(\boldsymbol{n}_{\Gamma_d}^T \boldsymbol{N}_d \boldsymbol{u}\right)^2 \left(\boldsymbol{\nabla} \boldsymbol{N}_w \boldsymbol{p}_w\right) \left(\boldsymbol{\nabla} \boldsymbol{N}_w\right)^T \boldsymbol{n}_{\Gamma_d}^T \boldsymbol{N}_d \mathrm{d}\Gamma \tag{A.28}$$

$$\boldsymbol{H}_{d,ww}^{cubic} = -\Delta t \int_{\Gamma_d} \frac{S_w^3}{12\mu_w} \left(\boldsymbol{n}_{\Gamma_d}^T \boldsymbol{N}_d \boldsymbol{u}\right)^3 \left(\boldsymbol{\nabla} \boldsymbol{N}_w\right)^T \boldsymbol{\nabla} \boldsymbol{N}_w - \frac{S_w^2}{4\mu_w} \left(\boldsymbol{n}_{\Gamma_d}^T \boldsymbol{N}_d \boldsymbol{u}\right)^3 \left(\boldsymbol{\nabla} \boldsymbol{N}_w \boldsymbol{p}_w\right) \frac{\partial S_w}{\partial p_c} \left(\boldsymbol{\nabla} \boldsymbol{N}_w\right)^T \boldsymbol{N}_w \mathrm{d}\Gamma \tag{A.29}$$

$$\boldsymbol{H}_{d,wn}^{cubic} = -\Delta t \int_{\Gamma_d} \frac{S_w^2}{4\mu_w} \left(\boldsymbol{n}_{\Gamma_d}^T \boldsymbol{N}_d \boldsymbol{u}\right)^3 \left(\boldsymbol{\nabla} \boldsymbol{N}_w \boldsymbol{p}_w\right) \frac{\partial S_w}{\partial p_c} \left(\boldsymbol{\nabla} \boldsymbol{N}_w\right)^T \boldsymbol{N}_n \mathrm{d}\Gamma \tag{A.30}$$

$$\boldsymbol{H}_{d,ns}^{cubic} = -\Delta t \int_{\Gamma_d} \frac{S_n^3}{4\mu_n} \left(\boldsymbol{n}_{\Gamma_d}^T \boldsymbol{N}_d \boldsymbol{u}\right)^2 \left(\boldsymbol{\nabla} \boldsymbol{N}_n \boldsymbol{p}_n\right) \left(\boldsymbol{\nabla} \boldsymbol{N}_n\right)^T \boldsymbol{n}_{\Gamma_d}^T \boldsymbol{N}_d \mathrm{d}\Gamma \tag{A.31}$$

$$\boldsymbol{H}_{d,nw}^{cubic} = -\Delta t \int_{\Gamma_d} \frac{S_n^2}{4\mu_n} \left(\boldsymbol{n}_{\Gamma_d}^T \boldsymbol{N}_d \boldsymbol{u}\right)^3 \left(\boldsymbol{\nabla} \boldsymbol{N}_n \boldsymbol{p}_n\right) \frac{\partial S_w}{\partial p_c} \left(\boldsymbol{\nabla} \boldsymbol{N}_n\right)^T \boldsymbol{N}_w \mathrm{d}\Gamma \tag{A.32}$$

$$\boldsymbol{H}_{d,nn}^{cubic} = -\Delta t \int_{\Gamma_d} \frac{S_n^3}{12\mu_n} \left(\boldsymbol{n}_{\Gamma_d}^T \boldsymbol{N}_d \boldsymbol{u}\right)^3 \left(\boldsymbol{\nabla} \boldsymbol{N}_n\right)^T \boldsymbol{\nabla} \boldsymbol{N}_n - \frac{S_w^2}{4\mu_w} \left(\boldsymbol{n}_{\Gamma_d}^T \boldsymbol{N}_d \boldsymbol{u}\right)^3 \left(\boldsymbol{\nabla} \boldsymbol{N}_w \boldsymbol{p}_w\right) \frac{\partial S_w}{\partial p_c} \left(\boldsymbol{\nabla} \boldsymbol{N}_n\right)^T \boldsymbol{N}_n \mathrm{d}\Gamma \tag{A.33}$$

for the volume-averaged bubbly flow by:

$$\boldsymbol{H}_{d,ws}^{bubbly} = -\Delta t \int_{\Gamma_d} \frac{\Delta t S_w}{4\left(S_w\mu_w + S_n\mu_n\right)} \left(\boldsymbol{n}_{\Gamma_d}^T \boldsymbol{N}_d \boldsymbol{u}^{t+\Delta t}\right)^2 \left(S_w \boldsymbol{\nabla} \boldsymbol{N}_w \boldsymbol{p}_w^{t+\Delta t} + S_n \boldsymbol{\nabla} \boldsymbol{N}_n \boldsymbol{p}_n^{t+\Delta t}\right) \left(\boldsymbol{\nabla} \boldsymbol{N}_w\right)^T \boldsymbol{n}_{\Gamma_d}^T \boldsymbol{N}_d \mathrm{d}\Gamma \tag{A.34}$$

$$\begin{aligned}\boldsymbol{H}_{d,ww}^{bubbly} = -\Delta t \int_{\Gamma_d} & \frac{1}{12\left(S_w\mu_w + S_n\mu_n\right)} \left(\boldsymbol{n}_{\Gamma_d}^T \boldsymbol{N}_d \boldsymbol{u}^{t+\Delta t}\right)^3 \Bigg(\Bigg(\left(S_w \boldsymbol{\nabla} \boldsymbol{N}_w \boldsymbol{p}_w + S_n \boldsymbol{\nabla} \boldsymbol{N}_n \boldsymbol{p}_n\right) \\ & \left(-\frac{\partial S_w}{\partial p_c} + \frac{-S_w}{S_w\mu_w + S_n\mu_n}\left(-\frac{\partial S_w}{\partial p_c}\mu_w + \frac{\partial S_w}{\partial p_c}\mu_n\right)\right) + S_w\left(-\frac{\partial S_w}{\partial p_c}\boldsymbol{\nabla} \boldsymbol{N}_w \boldsymbol{p}_w + \frac{\partial S_w}{\partial p_c}\boldsymbol{\nabla} \boldsymbol{N}_n \boldsymbol{p}_n\right)\Bigg) \left(\boldsymbol{\nabla} \boldsymbol{N}_w\right)^T \boldsymbol{N}_w \\ & + S_w^2 \left(\boldsymbol{\nabla} \boldsymbol{N}_w\right)^T \boldsymbol{\nabla} \boldsymbol{N}_w \Bigg) \mathrm{d}\Gamma\end{aligned} \tag{A.35}$$

$$\begin{aligned}\boldsymbol{H}_{d,wn}^{bubbly} = -\Delta t \int_{\Gamma_d} & \frac{1}{12\left(S_w\mu_w + S_n\mu_n\right)} \left(\boldsymbol{n}_{\Gamma_d}^T \boldsymbol{N}_d \boldsymbol{u}^{t+\Delta t}\right)^3 \Bigg(\Bigg(\left(S_w \boldsymbol{\nabla} \boldsymbol{N}_w \boldsymbol{p}_w + S_n \boldsymbol{\nabla} \boldsymbol{N}_n \boldsymbol{p}_n\right) \\ & \left(\frac{\partial S_w}{\partial p_c} + \frac{-S_w}{S_w\mu_w + S_n\mu_n}\left(\frac{\partial S_w}{\partial p_c}\mu_w - \frac{\partial S_w}{\partial p_c}\mu_n\right)\right) + S_w\left(\frac{\partial S_w}{\partial p_c}\boldsymbol{\nabla} \boldsymbol{N}_w \boldsymbol{p}_w - \frac{\partial S_w}{\partial p_c}\boldsymbol{\nabla} \boldsymbol{N}_n \boldsymbol{p}_n\right)\Bigg) \left(\boldsymbol{\nabla} \boldsymbol{N}_w\right)^T \boldsymbol{N}_n \\ & + S_w S_n \left(\boldsymbol{\nabla} \boldsymbol{N}_w\right)^T \boldsymbol{\nabla} \boldsymbol{N}_n \Bigg) \mathrm{d}\Gamma\end{aligned} \tag{A.36}$$

$$\boldsymbol{H}_{d,ns}^{bubbly} = -\Delta t \int_{\Gamma_d} \frac{\Delta t S_n}{4\left(S_w\mu_w + S_n\mu_n\right)} \left(\boldsymbol{n}_{\Gamma_d}^T \boldsymbol{N}_d \boldsymbol{u}^{t+\Delta t}\right)^2 \left(S_w \boldsymbol{\nabla} \boldsymbol{N}_w \boldsymbol{p}_w^{t+\Delta t} + S_n \boldsymbol{\nabla} \boldsymbol{N}_n \boldsymbol{p}_n^{t+\Delta t}\right) \left(\boldsymbol{\nabla} \boldsymbol{N}_w\right)^T \boldsymbol{n}_{\Gamma_d}^T \boldsymbol{N}_d \mathrm{d}\Gamma \tag{A.37}$$

$$\begin{aligned}\boldsymbol{H}_{d,nw}^{bubbly} = -\Delta t \int_{\Gamma_d} & \frac{1}{12\left(S_w\mu_w + S_n\mu_n\right)} \left(\boldsymbol{n}_{\Gamma_d}^T \boldsymbol{N}_d \boldsymbol{u}^{t+\Delta t}\right)^3 \Bigg(\Bigg(\left(S_w \boldsymbol{\nabla} \boldsymbol{N}_w \boldsymbol{p}_w + S_n \boldsymbol{\nabla} \boldsymbol{N}_n \boldsymbol{p}_n\right) \\ & \left(\frac{\partial S_w}{\partial p_c} + \frac{-S_n}{S_w\mu_w + S_n\mu_n}\left(-\frac{\partial S_w}{\partial p_c}\mu_w + \frac{\partial S_w}{\partial p_c}\mu_n\right)\right) + S_n\left(-\frac{\partial S_w}{\partial p_c}\boldsymbol{\nabla} \boldsymbol{N}_w \boldsymbol{p}_w + \frac{\partial S_w}{\partial p_c}\boldsymbol{\nabla} \boldsymbol{N}_n \boldsymbol{p}_n\right)\Bigg) \left(\boldsymbol{\nabla} \boldsymbol{N}_n\right)^T \boldsymbol{N}_w \\ & + S_n S_w \left(\boldsymbol{\nabla} \boldsymbol{N}_n\right)^T \boldsymbol{\nabla} \boldsymbol{N}_w \Bigg) \mathrm{d}\Gamma\end{aligned} \tag{A.38}$$

$$\begin{aligned}\boldsymbol{H}_{d,nn}^{bubbly} = -\Delta t \int_{\Gamma_d} & \frac{1}{12\left(S_w\mu_w + S_n\mu_n\right)} \left(\boldsymbol{n}_{\Gamma_d}^T \boldsymbol{N}_d \boldsymbol{u}^{t+\Delta t}\right)^3 \Bigg(\Bigg(\left(S_w \boldsymbol{\nabla} \boldsymbol{N}_w \boldsymbol{p}_w + S_n \boldsymbol{\nabla} \boldsymbol{N}_n \boldsymbol{p}_n\right) \\ & \left(-\frac{\partial S_w}{\partial p_c} + \frac{-S_n}{S_w\mu_w + S_n\mu_n}\left(\frac{\partial S_w}{\partial p_c}\mu_w - \frac{\partial S_w}{\partial p_c}\mu_n\right)\right) + S_n\left(\frac{\partial S_w}{\partial p_c}\boldsymbol{\nabla} \boldsymbol{N}_w \boldsymbol{p}_w - \frac{\partial S_w}{\partial p_c}\boldsymbol{\nabla} \boldsymbol{N}_n \boldsymbol{p}_n\right)\Bigg) \left(\boldsymbol{\nabla} \boldsymbol{N}_n\right)^T \boldsymbol{N}_n \\ & + S_n^2 \left(\boldsymbol{\nabla} \boldsymbol{N}_n\right)^T \boldsymbol{\nabla} \boldsymbol{N}_n \Bigg) \mathrm{d}\Gamma\end{aligned} \tag{A.39}$$

and for the separated flow model by:

$$\begin{aligned}\boldsymbol{H}_{d,ws}^{separated} &= -\Delta t \int_{\Gamma_d} \frac{1}{\mu_w} \left(\boldsymbol{n}_{\Gamma_d}^T \boldsymbol{N}_d \boldsymbol{u}\right)^2 \Bigg(\boldsymbol{\nabla} \boldsymbol{N}_w \boldsymbol{p}_w \left(\frac{1}{4} - \frac{3}{8} S_n + \frac{1}{8} S_n^3\right) \\ &+ \left(\boldsymbol{\nabla} \boldsymbol{N}_n \boldsymbol{p}_n - \boldsymbol{\nabla} \boldsymbol{N}_w \boldsymbol{p}_w\right) \left(\frac{3}{8} S_n - \frac{3}{4} S_n^2 + \frac{3}{8} S_n^3\right) \Bigg) \left(\boldsymbol{\nabla} \boldsymbol{N}_w\right)^T \boldsymbol{n}_{\Gamma_d}^T \boldsymbol{N}_d \mathrm{d}\Gamma\end{aligned} \tag{A.40}$$

$$\begin{aligned}\boldsymbol{H}_{d,ww}^{separated} &= -\Delta t \int_{\Gamma_d} \frac{1}{\mu_w} \left(\boldsymbol{n}_{\Gamma_d}^T \boldsymbol{N}_d \boldsymbol{u}\right)^3 \Bigg(\Bigg(\boldsymbol{\nabla} \boldsymbol{N}_w \boldsymbol{p}_w \left(\frac{1}{8} S_n^2 - \frac{1}{8}\right) + \left(\boldsymbol{\nabla} \boldsymbol{N}_n \boldsymbol{p}_n - \boldsymbol{\nabla} \boldsymbol{N}_w \boldsymbol{p}_w\right) \\ &\left(\frac{1}{8} - \frac{1}{2} S_n + \frac{3}{8} S_n^2\right) \Bigg) \frac{\partial S_w}{\partial p_c} \left(\boldsymbol{\nabla} \boldsymbol{N}_w\right)^T \boldsymbol{N}_w + \left(\frac{1}{12} - \frac{2}{8} S_n - \frac{1}{12} S_n^3 + \frac{1}{4} S_n^2\right) \left(\boldsymbol{\nabla} \boldsymbol{N}_w\right)^T \boldsymbol{\nabla} \boldsymbol{N}_w \Bigg) \mathrm{d}\Gamma\end{aligned} \tag{A.41}$$

$$\begin{aligned}\boldsymbol{H}_{d,wn}^{separated} &= \Delta t \int_{\Gamma_d} \frac{1}{\mu_w} \left(\boldsymbol{n}_{\Gamma_d}^T \boldsymbol{N}_d \boldsymbol{u}\right)^3 \Bigg(\Bigg(\boldsymbol{\nabla} \boldsymbol{N}_w \boldsymbol{p}_w \left(\frac{1}{8} S_n^2 - \frac{1}{8}\right) + \left(\boldsymbol{\nabla} \boldsymbol{N}_n \boldsymbol{p}_n - \boldsymbol{\nabla} \boldsymbol{N}_w \boldsymbol{p}_w\right) \\ &\left(\frac{1}{8} - \frac{1}{2} S_n + \frac{3}{8} S_n^2\right) \Bigg) \frac{\partial S_w}{\partial p_c} \left(\boldsymbol{\nabla} \boldsymbol{N}_w\right)^T \boldsymbol{N}_n + \left(\frac{1}{4} S_n^2 - \frac{1}{8} S_n - \frac{1}{8} S_n^3\right) \left(\boldsymbol{\nabla} \boldsymbol{N}_w\right)^T \boldsymbol{\nabla} \boldsymbol{N}_n \Bigg) \mathrm{d}\Gamma\end{aligned} \tag{A.42}$$

$$\begin{aligned}\boldsymbol{H}_{d,ns}^{separated} &= -\Delta t \int_{\Gamma_d} \frac{1}{\mu_w} \left(\boldsymbol{n}_{\Gamma_d}^T \boldsymbol{N}_d \boldsymbol{u}\right)^2 \Bigg(\frac{1}{12\mu_n} S_n^3 \boldsymbol{\nabla} \boldsymbol{N}_n \boldsymbol{p}_n + \frac{1}{8\mu_w} \boldsymbol{\nabla} \boldsymbol{N}_w \boldsymbol{p}_w \left(S_n - S_n^3\right) \\ &+ \frac{1}{4\mu_w} \left(\boldsymbol{\nabla} \boldsymbol{N}_n \boldsymbol{p}_n - \boldsymbol{\nabla} \boldsymbol{N}_w \boldsymbol{p}_w\right) \left(S_n^2 - S_n^3\right) \Bigg) \left(\boldsymbol{\nabla} \boldsymbol{N}_n\right)^T \boldsymbol{n}_{\Gamma_d}^T \boldsymbol{N}_d \mathrm{d}\Gamma\end{aligned} \tag{A.43}$$

$$\begin{aligned}\boldsymbol{H}_{d,nw}^{separated} &= \Delta t \int_{\Gamma_d} \left(\boldsymbol{n}_{\Gamma_d}^T \boldsymbol{N}_d \boldsymbol{u}\right)^3 \Bigg(\Bigg(- \frac{1}{4\mu_n} S_n^2 \boldsymbol{\nabla} \boldsymbol{N}_n \boldsymbol{p}_n + \frac{1}{\mu_w} \boldsymbol{\nabla} \boldsymbol{N}_w \boldsymbol{p}_w \left(\frac{3}{8} S_n^2 - \frac{1}{8}\right) \\ &+ \frac{1}{\mu_w} \left(\boldsymbol{\nabla} \boldsymbol{N}_n \boldsymbol{p}_n - \boldsymbol{\nabla} \boldsymbol{N}_w \boldsymbol{p}_w\right) \left(\frac{3}{4} S_n^2 - \frac{1}{2} S_n\right) \Bigg) \frac{\partial S_w}{\partial p_c} \left(\boldsymbol{\nabla} \boldsymbol{N}_n\right)^T \boldsymbol{N}_n \\ &+ \left(\frac{1}{8\mu_w} \left(S_n^3 - S_n\right) + \frac{1}{4\mu_w} \left(S_n^2 - S_n^3\right)\right) \left(\boldsymbol{\nabla} \boldsymbol{N}_n\right)^T \boldsymbol{\nabla} \boldsymbol{N}_w \Bigg) \mathrm{d}\Gamma\end{aligned} \tag{A.44}$$

$$\begin{aligned}\boldsymbol{H}_{d,nn}^{separated} &= -\Delta t \int_{\Gamma_d} \left(\boldsymbol{n}_{\Gamma_d}^T \boldsymbol{N}_d \boldsymbol{u}\right)^3 \Bigg(\Bigg(- \frac{1}{4\mu_n} S_n^2 \boldsymbol{\nabla} \boldsymbol{N}_n \boldsymbol{p}_n + \frac{1}{\mu_w} \boldsymbol{\nabla} \boldsymbol{N}_w \boldsymbol{p}_w \left(\frac{3}{8} S_n^2 - \frac{1}{8}\right) \\ &+ \frac{1}{\mu_w} \left(\boldsymbol{\nabla} \boldsymbol{N}_n \boldsymbol{p}_n - \boldsymbol{\nabla} \boldsymbol{N}_w \boldsymbol{p}_w\right) \left(\frac{3}{4} S_n^2 - \frac{1}{2} S_n\right) \Bigg) \frac{\partial S_w}{\partial p_c} \left(\boldsymbol{\nabla} \boldsymbol{N}_n\right)^T \boldsymbol{N}_n \\ &+ \left(\frac{1}{12\mu_n} S_n^3 + \frac{1}{4\mu_w} \left(S_n^2 - S_n^3\right)\right) \left(\boldsymbol{\nabla} \boldsymbol{N}_n\right)^T \boldsymbol{\nabla} \boldsymbol{N}_n \Bigg) \mathrm{d}\Gamma\end{aligned} \tag{A.45}$$

References

[1] B. Jha, R. Juanes, Coupled multiphase flow and poromechanics: A computational model of pore pressure effects on fault slip and earthquake triggering, Water Resources Research 50 (2014) 3776–3808. `doi:10.1002/2013WR015175`.

[2] B. Li, H. A. Tchelepi, Nonlinear analysis of multiphase transport in porous media in the presence of viscous, buoyancy, and capillary forces, Journal of Computational Physics 297 (2015) 104–131. `doi:10.1016/j.jcp.2015.04.057`.

[3] H. W. Zhang, B. A. Schrefler, Gradient-dependent plasticity model and dynamic strain localisation analysis of saturated and partially saturated porous media: one dimensional model, European Journal of Mechanics - A/Solids 19 (2000) 503–524. `doi:10.1016/S0997-7538(00)00177-7`.

[4] B. A. Schrefler, R. Scotta, A fully coupled dynamic model for two-phase fluid flow in deformable porous media, Computer Methods in Applied Mechanics and Engineering 190 (2001) 3223–3246. `doi:10.1016/S0045-7825(00)00390-X`.

[5] A. R. Khoei, T. Mohammadnejad, Numerical modeling of multiphase fluid flow in deforming porous media: A comparison between two- and three-phase models for seismic analysis of earth and rockfill dams, Computers and Geotechnics 38 (2011) 142–166. `doi:10.1016/j.compgeo.2010.10.010`.

[6] Y. Sieffert, O. Buzzi, F. Collin, Numerical study of shear band instability and effect of cavitation on the response of a specimen under undrained biaxial loading, International Journal of Solids and Structures 51 (2014) 1686–1696. `doi:10.1016/J.IJSOLSTR.2014.01.009`.

[7] A. Gajo, F. Cecinato, B. Loret, Deformable porous media saturated by three immiscible fluids: Constitutive modelling and simulations of injection and imbibition tests, Transport in Porous Media 116 (2017) 19–51. `doi:10.1007/s11242-016-0763-2`.

[8] Q. Deng, V. Ginting, B. McCaskill, P. Torsu, A locally conservative stabilized continuous Galerkin finite element method for two-phase flow in poroelastic subsurfaces, Journal of Computational Physics 347 (2017) 78–98. `doi:10.1016/J.JCP.2017.06.024`.

[9] M. R. Correa, M. A. Murad, A new sequential method for three-phase immiscible flow in poroelastic media, Journal of Computational Physics 373 (2018) 493–532. `doi:10.1016/J.JCP.2018.06.069`.

[10] S. E. Minkoff, C. M. Stone, S. Bryant, M. Peszynska, M. F. Wheeler, Coupled fluid flow and geomechanical deformation modeling, Journal of Petroleum Science and Engineering 38 (2003) 37–56.

[11] M. J. Blunt, Flow in porous media pore-network models and multiphase flow, Current Opinion in Colloid & Interface Science 6 (2001) 197–207. `doi:10.1016/S1359-0294(01)00084-X`.

[12] M. J. Blunt, M. D. Jackson, M. Piri, P. H. Valvatne, Detailed physics, predictive capabilities and macroscopic consequences for pore-network models of multiphase flow, Advances in Water Resources 25 (2002) 1069–1089. `doi:10.1016/S0309-1708(02)00049-0`.

[13] K. Khayrat, P. Jenny, A multi-scale network method for two-phase flow in porous media, Journal of Computational Physics 342 (2017) 194–210. `doi:10.1016/j.jcp.2017.04.023`.

[14] S. Salimzadeh, N. Khalili, A three-phase XFEM model for hydraulic fracturing with cohesive crack propagation, Computers and Geotechnics 69 (2015) 82–92. `doi:10.1016/j.compgeo.2015.05.001`.

[15] A. R. Khoei, N. Hosseini, T. Mohammadnejad, Numerical modeling of two-phase fluid flow in deformable fractured porous media using the extended finite element method and an equivalent continuum model, Advances in Water Resources 94 (2016) 510–528.

[16] J. Réthoré, R. de Borst, M.-A. Abellan, A two-scale model for fluid flow in an unsaturated porous medium with cohesive cracks, Computational Mechanics 42 (2008) 227–238. `doi:10.1007/s00466-007-0178-6`.

[17] T. Mohammadnejad, A. R. Khoei, Hydro-mechanical modeling of cohesive crack propagation in multiphase porous media using the extended finite element method, International Journal for Numerical and Analytical Methods in Geomechanics 37 (2013) 1247–1279.

[18] I. Y. Akkutlu, Y. Efendiev, M. Vasilyeva, Y. Wang, Multiscale model reduction for shale gas transport in poroelastic fractured media, Journal of Computational Physics 353 (2018) 356–376. `doi:10.1016/J.JCP.2017.10.023`.

[19] H. Hoteit, A. Firoozabadi, Numerical modeling of two-phase flow in heterogeneous permeable media with different capillarity pressures, Advances in Water Resources 31 (2008) 56–73. `doi:10.1016/J.ADVWATRES.2007.06.006`.

[20] K. Brenner, M. Groza, L. Jeannin, R. Masson, J. Pellerin, Immiscible two-phase Darcy flow model accounting for vanishing and discontinuous capillary pressures: application to the flow in fractured porous media, Computational Geosciences 21 (2017) 1075–1094. `doi:10.1007/s10596-017-9675-7`.

[21] E. Unsal, S. K. Matthäi, M. J. Blunt, Simulation of multiphase flow in fractured reservoirs using a fracture-only model with transfer functions, Computational Geosciences 14 (2010) 527–538. `doi:10.1007/s10596-009-9168-4`.

[22] S. Lee, A. Mikelic, M. F. Wheeler, T. Wick, Phase-field modeling of two phase fluid filled fractures in a poroelastic medium, Multiscale Modeling and Simulation 16 (4) (2018) 1542–1580.

[23] S. M. Ghiaasiaan, S. I. Abdel-Khalik, Two-phase flow in microchannels, Advances in Heat Transfer 34 (2001) 145–254. `doi:10.1016/S0065-2717(01)80012-5`.

[24] P. G. Ranjith, S. K. Choi, M. Fourar, Characterization of two-phase flow in a single rock joint, International Journal of Rock Mechanics and Mining Sciences 43 (2006) 216–223. `doi:10.1016/j.ijrmms.2005.06.001`.

[25] S. Raza, S. H. Hejazi, I. D. Gates, Two phase flow of liquids in a narrow gap: Phase interference and hysteresis, Physics of Fluids 28 (7) (2016) 074102. `doi:10.1063/1.4953238`.

[26] S. Shad, B. B. Maini, I. D. Gates, Effect of gap and flow orientation on two-phase flow in an oil-wet gap: Relative permeability curves and flow structures, International Journal of Multiphase Flow 57 (2013) 78–87. `doi:10.1016/j.ijmultiphaseflow.2013.07.004`.

[27] W. J. Layton, F. Schieweck, I. Yotov, Coupling fluid flow with porous media flow, SIAM Journal on Numerical Analysis 40 (6) (2002) 2195–2218.

[28] I. Ambartsumyan, E. Khattatov, T. Nguyen, I. Yotov, Flow and transport in fractured poroelastic media, GEM - International Journal on Geomathematics 10 (1) (2019) 1–34.

[29] M. Bai, F. Meng, D. Elsworth, Y. Abousleiman, J.-C. Roegiers, Numerical modelling of coupled flow and deformation in fractured rock specimens, International Journal for Numerical and Analytical Methods in Geomechanics 23 (2) (1999) 141–160.

[30] M. Bukac, I. Yotov, P. Zunino, Dimensional model reduction for flow through fractures in poroelastic media, ESAIM: Mathematical Modelling and Numerical Analysis 51 (4) (2016) 1429–1471. `doi:10.1051/m2an/2016069`.

[31] P. Angot, F. Boyer, F. Hubert, Asymptotic and numerical modelling of flows in fractured porous media, ESAIM: Mathematical Modelling and Numerical Analysis 43 (2) (2009) 239–275.

[32] H. Hajibeygi, D. Karvounis, P. Jenny, A hierarchical fracture model for the iterative multiscale finite volume method,

Journal of Computational Physics 230 (2011) 8729–8743.

[33] V. Martin, J. Jaffré, J. E. Roberts, Modeling Fractures and Barriers as Interfaces for Flow in Porous Media, SIAM Journal on Scientific Computing 26 (5) (2005) 1667–1691.

[34] J. M. Segura, I. Carol, Coupled HM analysis using zero-thickness interface elements with double nodes. Part I: Theoretical model, International Journal for Numerical and Analytical Methods in Geomechanics 32 (18) (2008) 2083–2101.

[35] R. de Borst, J. Réthoré, M. A. Abellan, A numerical approach for arbitrary cracks in a fluid-saturated medium, Archive of Applied Mechanics 75 (2006) 505–606.

[36] N. Watanabe, W. Wang, J. Taron, U. J. Görke, O. Kolditz, Lower-dimensional interface elements with local enrichment: application to coupled hydro-mechanical problems in discretely fractured porous media, International Journal for Numerical Methods in Engineering 90 (8) (2012) 1010–1034.

[37] J. Réthoré, R. de Borst, M.-A. Abellan, A two-scale approach for fluid flow in fractured porous media, International Journal for Numerical Methods in Engineering 71 (2006) 780–800. `doi:10.1002/nme.1962`.

[38] R. de Borst, Computational Methods for Fracture in Porous Media, Elsevier, 2017.

[39] V. Girault, M. F. Wheeler, B. Ganis, M. E. Mear, A lubrication fracture model in a poro-elastic medium, Mathematical Models and Methods in Applied Sciences 25 (4) (2015) 587–645.

[40] B. Ganis, V. Girault, M. Mear, G. Singh, M. F. Wheeler, Modeling Fractures in a Poro-Elastic Medium, Oil and Gas Science and Technology 69 (4) (2014) 515–528.

[41] B. Ganis, M. E. Mear, A. Sakhaee-Pour, M. F. Wheeler, T. Wick, Modeling fluid injection in fractures with a reservoir simulator coupled to a boundary element method, Computational Geosciences 18 (5) (2014) 613–624.

[42] E. W. Remij, J. J. C. Remmers, J. M. Huyghe, D. M. J. Smeulders, An investigation of the step-wise propagation of a mode-II fracture in a poroelastic medium, Mechanics Research Communications 80 (2017) 10–15.

[43] R. de Borst, Fluid flow in fractured and fracturing porous media: A unified view, Mechanics Research Communications 80 (2017) 47–57.

[44] J. Vignollet, S. May, R. de Borst, Isogeometric analysis of fluid-saturated porous media including flow in the cracks, International Journal for Numerical Methods in Engineering 108 (2016) 990–1006. `doi:10.1002/nme.5242`.

[45] T. Hageman, R. de Borst, Flow of non-Newtonian fluids in fractured porous media: Isogeometric vs standard finite element discretisation, International Journal for Numerical and Analytical Methods in Geomechanics 43 (2019) 2020–2037.

[46] T. Hageman, K. M. Pervaiz Fathima, R. de Borst, Isogeometric analysis of fracture propagation in saturated porous media due to a pressurised non-Newtonian fluid, Computers and Geotechnics 112 (2019) 272–283.

[47] E. W. Remij, J. J. C. Remmers, J. M. Huyghe, D. M. J. Smeulders, The enhanced local pressure model for the accurate analysis of fluid pressure driven fracture in porous materials, Computer Methods in Applied Mechanics and Engineering 286 (2015) 293–312.

[48] K. M. Pervaiz Fathima, R. de Borst, Implications of single or multiple pressure degrees of freedom at fractures in fluid-saturated porous media, Engineering Fracture Mechanics 213 (2019) 1–20.

[49] M. T. van Genuchten, A closed-form equation for predicting the hydraulic conductivity of unsaturated soils, Soil Science Society of America Journal 44 (1980) 892–898.

[50] O. Dury, U. Fischer, R. Schulin, A comparison of relative nonwetting-phase permeability models, Water Resources Research 35 (1999) 1481–1493.

[51] F. Irzal, J. J. C. Remmers, C. V. Verhoosel, R. de Borst, An isogeometric analysis Bézier interface element for mechanical and poromechanical fracture problems, International Journal for Numerical Methods in Engineering 97 (2014) 608–628. `doi:10.1002/nme.4615`.

[52] J. Vignollet, S. May, R. de Borst, On the numerical integration of isogeometric interface elements, International Journal for Numerical Methods in Engineering 102 (2015) 1733–1749. `doi:10.1002/nme.4867`.

[53] M. J. Nicholl, H. Rajaram, R. J. Glass, Factors controlling satiated relative permeability in a partially-saturated horizontal fracture, Geophysical Research Letters 27 (3) (2000) 393–396. `doi:10.1029/1999GL006083`.

[54] B. Berkowitz, Characterizing flow and transport in fractured geological media: A review, Advances in Water Resources 25 (8-12) (2002) 861–884.

[55] T. K. Tokunaga, J. Wan, Water film flow along fracture surfaces of porous rock, Water Resources Research 33 (6) (1997) 1287–1295.

[56] S. Shad, I. D. Gates, Multiphase Flow in Fractures: Co-Current and Counter-Current Flow in a Fracture, in: Canadian International Petroleum Conference, Petroleum Society of Canada, 2008, pp. 17–19.

[57] F. Irzal, J. J. C. Remmers, C. V. Verhoosel, R. de Borst, Isogeometric finite element analysis of poroelasticity, International Journal for Numerical and Analytical Methods in Geomechanics 37 (2013) 1891–1907. `doi:10.1002/nag.2195`.

[58] T. J. R. Hughes, J. A. Cottrell, Y. Bazilevs, Isogeometric analysis: CAD, finite elements, NURBS, exact geometry and mesh refinement, Computer Methods in Applied Mechanics and Engineering 194 (2005) 4135–4195. `doi:10.1016/J.CMA.2004.10.008`.

[59] M. J. Borden, M. A. Scott, J. A. Evans, T. J. R. Hughes, Isogeometric finite element data structures based on Bézier extraction of NURBS, International Journal for Numerical Methods in Engineering 87 (2011) 15–47. `doi:10.1002/nme.2968`.

[60] D. Chapelle, K. J. Bathe, The inf-sup test, Computers & Structures 47 (1993) 537–545. `doi:10.1016/0045-7949(93)90340-J`.

[61] T. J. R. Hughes, Multiscale phenomena: Green's functions, the Dirichlet-to-Neumann formulation, subgrid scale models, bubbles and the origins of stabilized methods, Computer Methods in Applied Mechanics and Engineering 127 (1995) 387–401. `doi:10.1016/0045-7825(95)00844-9`.

[62] R. Juanes, T. W. Patzek, Multiscale-stabilized finite element methods for miscible and immiscible flow in porous media,

Journal of Hydraulic Research 42 (2004) 131–140. `doi:10.1080/00221680409500056`.

[63] R. Juanes, A variational multiscale finite element method for multiphase flow in porous media, Finite Elements in Analysis and Design 41 (2005) 763–777. `doi:10.1016/J.FINEL.2004.10.008`.

[64] A. Truty, A Galerkin/leastsquares finite element formulation for consolidation, International Journal for Numerical Methods in Engineering 52 (2001) 763–786. `doi:10.1002/nme.224`.

[65] J. Vignollet, L. Kaczmarczyk, C. J. Pearce, A Galerkin least-square stabilisation technique for hyperelastic biphasic soft tissue, Computers & Structures 118 (2013) 109–114. `doi:10.1016/J.COMPSTRUC.2012.10.010`.

[66] W. Li, C. Wei, Stabilized low-order finite elements for strongly coupled poromechanical problems, International Journal for Numerical Methods in Engineering 115 (2018) 531–548. `doi:10.1002/nme.5815`.

[67] G. Meschke, S. Grasberger, Numerical modeling of coupled hygromechanical degradation of cementitious materials, Journal of Engineering Mechanics 129 (2003) 383–392. `doi:10.1061/(ASCE)0733-9399(2003)129:4(383)`.